PHOTOACOUSTIC IMAGING FOR PROSTATE BRACHYHERAPY

by

Leo Lijia Pan

B.Sc., The University of British Columbia, 2010

A THESIS SUBMITTED IN PARTIAL FULFILLMENT OF

THE REQUIREMENTS FOR THE DEGREE OF

MASTER OF APPLIED SCIENCE

in

THE FACULTY OF GRADUATE AND POSTDOCTORAL STUDIES

(Electrical and Computer Engineering)

THE UNIVERSITY OF BRITISH COLUMBIA

(Vancouver)

July 2014

Abstract

Photoacoustic (PA) imaging is an emerging imaging modality that relies on the PA effect. The PA effect is caused by exposing an optically absorbing sample to near-infrared light which causes the sample to experience a temporary temperature increase through optical absorption. The heated region undergoes thermoelastic expansion and produces an abrupt and localized pressure change. This change results in a transient PA wave that propagates out toward the sample surface for collection by an ultrasound (US) transducer. Through image reconstruction, the optical property of the sample can be obtained.

PA imaging is promising in detecting brachytherapy seeds during prostate brachytherapy. The high absorption coefficient of the metallic seeds leads to high PA imaging contrast. One major drawback is the limited imaging depth due to high optical attenuation of the excitation light in tissue. One of the goals of this thesis is to conduct initial feasibility tests of enhancing the PA contrast through brachytherapy seeds modifications. Seed coated with a contrast enhancing material shows an increase of 18 dB in signal-to-noise ratio (SNR) and two time increase in the imaging depth (5 cm). Another method of silver coating leads to a 5 dB improvement in the SNR of the modified seeds. An alternative approach in using dyed ethanol solution as a contrast enhancing agent by filling the spaces between two seeds is also reported. The result showed improvement comparable to the black paint method.

Another goal is to propose a novel method of tissue typing in PA imaging. A temperature change in tissue can lead to changes of several tissue parameters which can be used for tissue typing. One of the parameters is the speed of sound in tissue, which increases in water-based non-fatty tissue and decreases in fatty tissue as temperature is raised. We show that on average, 6.9 ± 1.5 %/min increase and 4.2 ± 1.5 %/min decrease in PA intensity are observed in porcine liver and bovine fat samples respectively through one minute of laser heating. These results demonstrate that by analyzing the PA intensity change of the illuminated sample, one can extract characteristic information that can lead to tissue type differentiation.

Preface

Part of work done in Chapter 2 was contributed by Hamid Moradi. He made the necessary connector in relaying the trigger signal from the function generator to the laser.

Part of the work done in Chapter 3 has been published. L. Pan, A. Baghani, R. Rohling, P. Abolmaesumi, S. Salcudean, and S. Tang, "Improving photoacoustic imaging contrast of brachytherapy seeds," in the proceedings of *SPIE* 8581, Photons Plus Ultrasound: Imaging and Sensing 2013, 85814B (March, 2013). I conducted all the experiments, analyzed the results, and wrote the manuscript.

Part of the work done in Chapter 4 has been published. L. Pan, R. Rohling, P. Abolmaesumi, S. Salcudean, and S. Tang, "Differentiating fatty and non-fatty tissue using photoacoustic imaging", in the proceedings of *SPIE* 8943, Photons Plus Ultrasound: Imaging and Sensing 2014, 894354 (March, 2014). I have conducted all the experiments, analyzed the results, and wrote the manuscript.

Table of Contents

List of Tables

List of Figures

List of Abbreviations

CT	Computed tomography
MRI	Magnetic resonance imaging
US	Ultrasound
PA	Photoacoustic
OA	Optoacoustic
PAT	Photoacoustic tomography
TRUS	Transrectal ultrasound
TMFP	Transport mean free path
HbO_2	Oxy-haemoglobin
HHb	Deoxy-haemoglobin
OPO	Optical parametric oscillator
ND:YAG	Neodymium-doped yttrium aluminum garnet
PSF	Point-spread function
FWHM	Full-width-at-half-max
FOV	Field of view
NIR	Near-infrared
PVC	Poly-vinyl chloride
SNR	Signal-to-noise ratio
ROI	Region of interest

Acknowledgements

I would like to express my appreciation to my supervisors, Dr. Robert Rohling, Dr. Tim Salcudean, and Dr. Shuo Tang for your continuous guidance and support. Special thanks to Dr. Tang for the direction and motivation given at the weekly group meeting. I am also grateful to be given an opportunity by Dr. Rohling to work as a Co-op student in your lab. Without it, I would never have known the wonderful world of medical imaging, and for that I am forever thankful.

I would also like to thank every single member of the Biophotonics and Robotic Control laboratories for their selfless assistances and support throughout the years.

Leo Lijia Pan

University of British Columbia

June 2014

This thesis is dedicated to my family for the unconditional love every step of the way.

Chapter 1: Introduction

Technological advancements in medical imaging have given physicians and technicians important tools to diagnose diseases noninvasively. Standard modalities employed in current diagnostic imaging include x-ray, x-ray computed tomography (CT), magnetic resonance imaging (MRI), ultrasonography (US), and various optical imaging modalities. Each modality can give a unique set of information about tissues. For example, x-ray and CT provide excellent contrast between soft tissue and bones in the human body with deep imaging penetration. However, these two modalities expose the patients to potentially harmful ionizing radiations. MRI, on the other hand, utilizes non-ionizing magnetic field to generate high resolution and strong contrast between soft tissues which cannot be achieved with x-ray or CT. The downside of MRI is its high operation and maintenance cost and low mobility. Ultrasonography, on the other hand, is a highly mobile and relatively inexpensive imaging modality that can provide large imaging depth as well as good resolution. Conventional US relies on the difference in acoustic impedance (product of speed of sound and density) to generate contrast, which can suffer in soft tissues that have low variations in the impedance value. Optical imaging can provide arguably the highest resolution amongst the various modalities with the use of non-ionizing near-infrared light. The major drawback of optical imaging is its shallow imaging depth due to the high optical attenuation in tissue, severely limiting the clinical application.

Photoacoustic (PA) imaging is a hybrid modality between US and optical imaging. It is emerging as a highly promising imaging modality in recent years. The

inherent multimodal property of PA imaging allows it to benefit from both worlds of acoustics and optics, making it a viable candidate for many applications. Since its inception, PA imaging has been widely researched for various application areas such as skin, vasculature, breast, brain, and prostate [1–5]. This thesis focuses on using PA imaging for prostate-related application. In this chapter, a brief history of PA imaging followed by a general summary of the various PA imaging systems currently being researched are presented. Advantages and challenges faced by PA imaging are also discussed, which lead to the motivation of our work. The chapter concludes with an outline of the entire thesis.

1.1 A brief history

PA imaging relying on the principle of PA, or optoacoustic (OA) effect was first discovered separately by Tyndall and Bell in 1880 [6,7]. Sound wave was generated from either a solid or gaseous material upon being irradiated by periodically modulated light. It was also observed that the resulting acoustic signal had clear dependence on the material of the sample, which was attributed to the variation in the optical absorption of the sample. The PA effect provided a way for measuring spectra beyond the visible regime otherwise undetectable at that time. In spite of the novelty and potential of such technique, research on the PA effect remained relatively inactive until the invention of the laser in the 1960s. High power, well controlled directionality, and spectral purity provided by the laser gave researchers the means to consistently generate reliable light source for excitation. This brought much needed interest back to the PA field. The first

wave of research on PA centered mainly on gas analysis and photochemical studies [8,9]. Applying the PA effect for imaging was not realized until 1980 when Bowen published his proof of concept for the potential of PA imaging in biological tissues [10]. By the turn of the millennium, a series of PA imaging studies of various applications were published [3,11–13]. The popularity of PA imaging for diagnostic as well as therapeutic medicine has grown rapidly since.

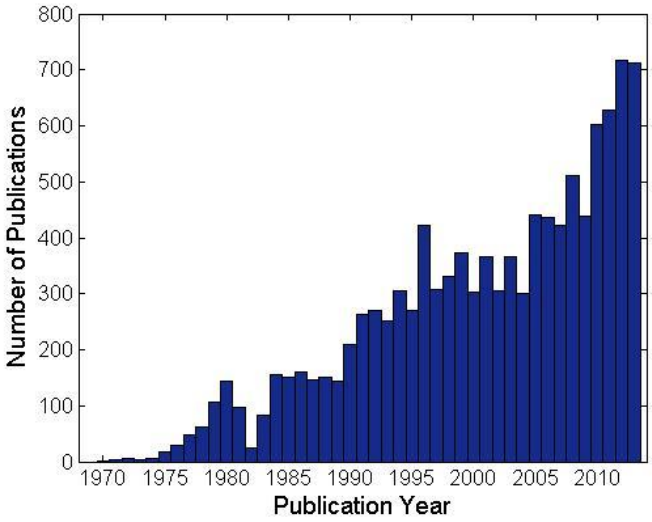

Figure 1.1: Number of publications containing the keywords "photoacoustic" or "optoacoustic" from 1970 until present. The numbers are tabulated with search results gathered on Web of Science (Thomson Reuters, USA).

1.2 Photoacoustic imaging system

The most essential components of any PA imaging system are the light source and the US transducer. The former is to successfully generate the PA effect, and the latter is to receive the PA waves caused by the PA effect. Over the years, many innovations and optimizations have been made to transfer the PA imaging technique into a clinically viable imaging modality.

PA tomography (PAT) is currently the most common configuration due to its simplicity and inexpensiveness. The simplest case of PAT uses a single US transducer attached to a mechanical scanning stage, which acquires a set of PA waves at each point in space as the transducer is scanned circularly around the sample as shown in Figure 1.2. A pulsed laser with large beam diameter is directed at the sample to generate PA waves from a large volume. A 2D image can be reconstructed from the recorded data by applying the standard back-projection algorithm [14]. Due to the requirement of a water bath for 360^{o} scanning, such a setup has limited clinical application and is usually used for small-animal imaging [4,15–17]. Yang et al. use a modified version of this setup by replacing the single transducer with a linear array transducer in order to gather more PA waves at each scanning position [18]. Although such a PAT system can provide relatively high resolution images, it suffers from long acquisition time due to the mechanical scanning process.

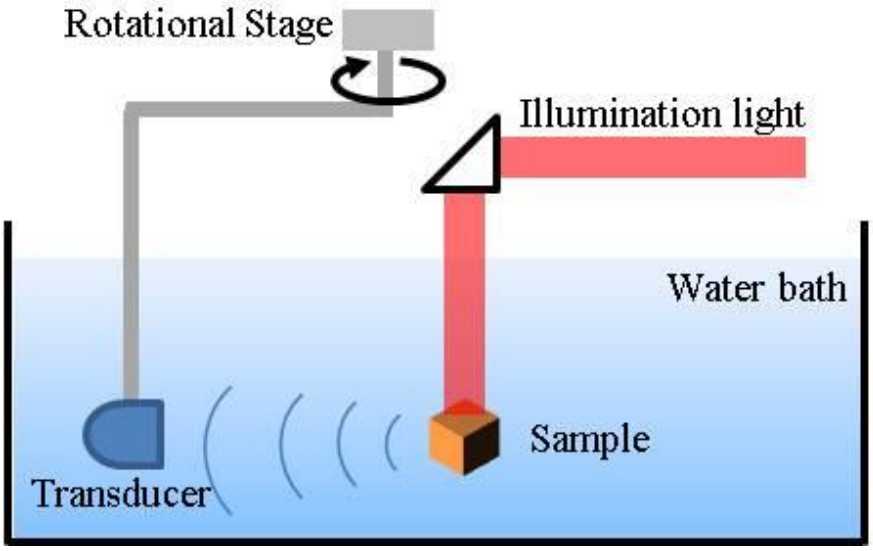

Figure 1.2: A simplified drawing of a single transducer PAT system setup

Recently, several groups have published modified PAT system targeted at breast imaging [19,20]. In these approaches, either a curved array or a hemispherical array of transducers is employed to capture PAT of the breast. A hemispherical transducer and the detected PA image are shown in Figure 1.3. The sensitivity of the system is shown to be comparable to x-ray mammography, and it can acquire images at around 5 Hz. Such setup, however, has severely restricted applicability since it requires the sample to be accessible from a large set of angles.

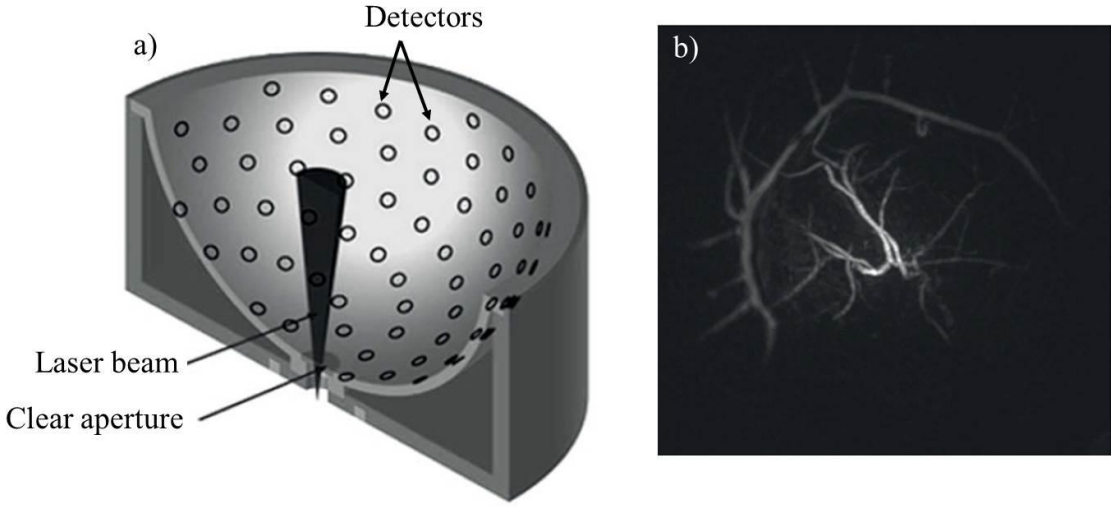

Figure 1.3 (a) hemispherical detector used in breast imaging, and (b) resulting PA image of the blood vessels within the breast. Source: Paul Beard, "Biomedical photoacoustic imaging", Figure 4 (a) and (c), © 2011 The Royal Society [20].

The last group of PAT systems uses a commercially available US transducer, typically a linear array. The excitation light source is usually delivered by optical fibres physically coupled to the side of the US transducer as shown in Figure 1.4. Such a system has lower cost, high acquisition speed, and can be easily integrated with conventional US system for multimodal imaging since both systems share the same

transducer. The main drawback is the lower imaging quality due to a lack of a full-angle view of the targeted area. Unlike the previous PAT configuration, this setup is designed for imaging features that cannot be imaged from multiple angles. Such a configuration is called the limited-view PAT system, while the previous ones are known as the full-view PAT systems. One example of the limited-view PAT is the system for *in-vivo* detection of skin melanoma and the surrounding vasculatures [1].

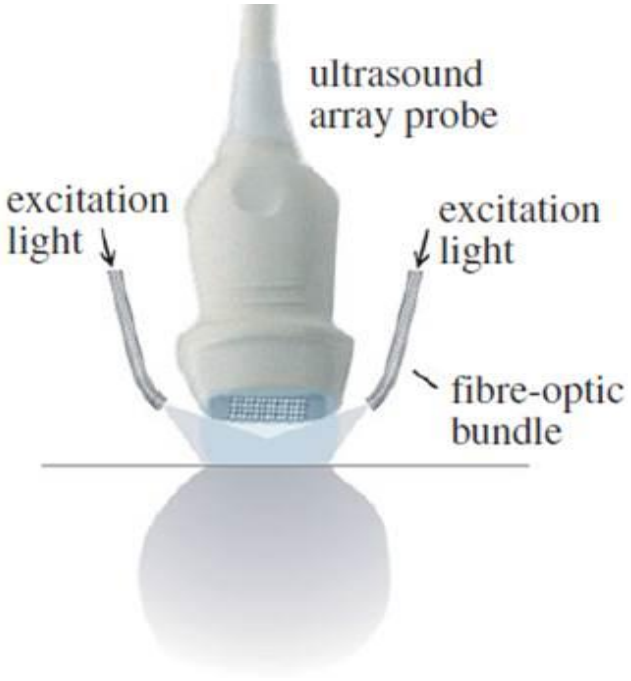

Figure 1.4: Drawing of a single linear array PAT system with excitation light delivered through fibres attached to the transducer. Source: Paul Beard, "Biomedical photoacoustic imaging", Figure 7 (a), © 2011 The Royal Society [20].

1.3 Photoacoustic imaging in prostate brachytherapy

A clinical application that is garnering attention in the use of limited-view PAT is urology. In particular, real-time imaging during prostate brachytherapy is of great interest to researchers. Brachytherapy is a form of radiotherapy where a number of radiating

sources are planted into and around the targeted cancerous region for localized and long-term radiation treatment [22]. Each radiating source is called a “seed”, which resembles a tiny metallic cylinder that encloses the radiating source inside. During prostate brachytherapy, these seeds are inserted into the targeted area. Accurate placement of the seeds according to the preoperative dosimetric treatment plan is essential in delivering a sufficient dose to the cancerous regions with a minimal dose to healthy tissues. The current standard modality used for intraoperative monitoring of the seeds placement is transrectal US (TRUS) imaging [23].

PA imaging is a viable candidate for imaging seeds due to its absorption-based imaging principle. Since PA contrast is generated through the PA effect, which in short is a process of converting photon energy first to thermal energy and then to acoustic energy, the optical absorption coefficient of the sample determines the conversion efficiency between photon energy and thermal energy. Several groups have shown that PA imaging of brachytherapy seeds is a viable method since the optical absorption difference between metal and soft tissue is larger than the corresponding acoustic impedance difference which determines the contrast in US imaging [5,24–26].

1.4 Problem statement and motivation

Despite the high contrast in seed imaging, challenges still exist with PA brachytherapy imaging and they are mainly twofold: shallow imaging depth and limited-view angle. A PA system has deeper imaging depth than most of the optical imaging modalities while maintaining relatively high resolution since the received PA signals are

in the form of acoustic waves. This does not necessarily mean that PA imaging can reach the same depth as an US system. PA imaging depth is still ultimately constrained by the penetration depth of excitation photons. Although it is not required for the penetrating photons to be well focused in order to achieve high resolution, it is still essential for the photons to deliver enough energy to generate the PA effect. In practice, brachytherapy seeds are placed as far as 7 cm away from the TRUS probe. The depth constraint coupled with the limited-view problem pose a serious challenge in PA imaging of the deeper brachytherapy seeds. Many groups have proposed modified reconstruction algorithms for limited-view PAT imaging in order to increase the image quality as well as penetration depth [27–30].

The focus of the first part of this thesis is on improving the PA imaging depth of brachytherapy seeds by modifying the seeds directly. This approach was motivated by the use of nanoparticles as a contrast enhancing agent in PA imaging [31]. The methodology for coating the seeds with contrast enhancing material is investigated and presented. The aim is to devise an efficient coating scheme that can allow deeper PA imaging depth in tissue. If successful, the PA imaging depth can be improved without any added hardware cost (e.g. for a better transducer) or increased computational time in post-processing.

The second part of the thesis outlines our work on an intensity-based tissue typing method using PA imaging. Previously, tissue typing has been reported by analyzing a time series data which is a set of continuously acquired US B-mode frames over a period of several seconds [32]. The thermal effect induced by the US beam is attributed as one

of the possible causes for tissue dependent variations in the time series data. We hypothesize that by capturing the time series data in PA imaging, tissue typing may also be a possibility since thermal effect by the laser could be more significant than by the US. Moreover, the speed of sound c in tissue is reported to have a temperature dependence that is characteristic to the type of tissues [33]. In pulse-echo US imaging, the change in c is observed in the temporal shift of the reflected signals, and groups have successfully measured temperature change in biological tissue by analyzing such shift [34–36]. The change in c is detected differently in PA imaging. The initial amplitude of the PA wave caused by the PA effect is shown to be proportional to c^2. Therefore, by analyzing the PA signal intensity change as the tissue temperature is raised we hope to extract tissue specific information from the PA data.

In this thesis, firstly a PA system is developed using a commercial US system for limited-view PAT imaging. Secondly, methods of enhancing PA contrast of brachytherapy seeds are investigated, and the improved performance of such seeds is demonstrated on our PA system. Lastly, a novel method of tissue typing using PA imaging is proposed and the results presented.

1.5 Organization of the thesis

Chapter 1: A brief overview of the theoretical background of PA imaging is given. Literature review on the current state of PA imaging is conducted. Finally, challenges faced with PA imaging are discussed and our goals for this thesis are proposed.

Chapter 2: Theoretical background with regard to PA imaging is presented. Aspects such as generation, propagation, attenuation, and mechanisms of contrast are discussed.

Chapter 3: The PA imaging system setup developed is introduced. Key changes made to the system for optimization and improvements are presented. The reconstruction algorithm employed for obtaining PA images is discussed. PA images of phantoms are acquired to characterize the system performance and imaging quality.

Chapter 4: PA imaging for detecting brachytherapy seeds is presented. Specifically, methods of improving the PA contrast of the seeds are reported and the results verified by the PA imaging system.

Chapter 5: A novel method of intensity-based tissue typing using PA imaging is presented. The analysis method and the results of such method performed on two tissue types are presented and discussed.

Chapter 6: The concluding chapter summarizes the work presented in the thesis and discusses the possible future directions of the project.

Chapter 2: Photoacoustic Theory

PA imaging is an emerging medical imaging technique that obtains the optical absorption information of the sample through the detection of acoustic waves produced by the PA effect. The PA effect is caused by exposing an optically absorbing sample to electromagnetic pulses (e.g. near-infrared light for biological tissue imaging), which causes the sample to experience a temporary temperature increase due to absorption. The heated region undergoes thermoelastic expansion and produces an abrupt and localized pressure change. This change results in a transient PA wave that propagates from the excitation region out toward the surface of the sample for collection by a US transducer. Unlike conventional US, the collected acoustic waves contain optical information of the sample. Therefore, PA imaging is considered to be a hybrid modality that measures the optical information (optical regime) carried by acoustic waves (acoustic regime). In this chapter, an overview on the theoretical background of PA imaging is presented.

2.1 Thermal and stress confinement

In order to generate the PA effect in a tissue sample, a short laser pulse on the order of nanoseconds is usually delivered onto the sample. There are two physical conditions, known as the thermal and stress confinements, that must be fulfilled for successful generation of the PA effect, and the laser pulse width needs to be sufficiently short to meet these conditions. Equation 2.1 describes the dissipation time scale of the absorbed laser energy through thermal conduction in the tissue sample [37]:

$$\boldsymbol{\tau_{th}} = \frac{\boldsymbol{L_p^2}}{\boldsymbol{4D_T}} \tag{2.1}$$

where L_p is the characteristic linear dimension of the absorption structure, and D_T is the thermal diffusivity of the sample. For soft tissues, D_T is typically around 1.4×10^{-7} m^2/s [38]. Considering that the typical imaging resolution of a PA imaging system being at millimeter to sub-millimeter range, L_p = 50 μm is a reasonable lower limit approximation of tissue structure size that can be resolved. This leads to an estimated thermal dissipation time, τ_{th}, of several hundred microseconds. Thermal confinement states that the pulse width of the illumination light needs to be shorter than τ_{th} in order to neglect the effect of heat diffusion during the excitation process. Otherwise, no heat can be built up quickly enough to result in a localized temperature increase. The second condition, stress confinement, is related to the stress relaxation time in tissue described by:

$$\boldsymbol{\tau_s} = \frac{\boldsymbol{L_p}}{\boldsymbol{c}} \tag{2.2}$$

where *c* is the speed of sound in the medium. Using the average speed of sound value in soft tissue of 1540 m/s and L_p mentioned earlier, the stress relaxation time τ_s is measured in the tens of nanoseconds. Once the pulse width of the light is shorter than τ_s, the stress confinement condition is met where high thermoelastic pressure can be rapidly built up before stress relaxation takes place. This is why a laser pulse on the time scale of nanoseconds is necessary to generate the PA effect.

2.2 Photoacoustic wave generation

Once the thermal and stress confinements conditions detailed above are satisfied, the sample excited by a delta laser pulse undergoes a localized pressure change described by:

$$\boldsymbol{p_0 = \mu_a F \left(\frac{\beta c^2}{C_p}\right) = \mu_a F \Gamma} \tag{2.3}$$

where μ_a is the optical absorption coefficient of the sample in cm^{-1}, F is the local optical fluence in mJ/cm^2, β is the isobaric volume expansion coefficient in K^{-1}, C_p is the specific heat capacity at constant pressure in J/(g·K), and c is the speed of sound. The terms enclosed in parenthesis in Equation 2.3 make up a dimensionless parameter called the Grueneisen parameter, Γ. This parameter relates the pressure change p_0 to the deposited optical energy F, and is measured to be ~0.8 in fatty tissue and ~0.2 in blood [39].

The initial pressure rise depends on the optical absorption and the Grueneisen parameter, assuming the local laser fluence rate is constant over the imaging area. In tissue, the variation in μ_a among different constituents is much larger than that of the Grueneisen parameter, and therefore the key information carried in the PA wave is the optical property (μ_a) of the sample.

2.3 Photoacoustic wave propagation

The propagation of a PA wave $p(\boldsymbol{r}, t)$ at position $\boldsymbol{r}$ and time t generated from an initial pressure rise of $p_0(\boldsymbol{r})$ is governed by the generalized wave equation:

$$\left(\nabla^2 - \frac{1}{c^2}\frac{\partial^2}{\partial t^2}\right) p(r,t) = -\frac{p_0(r)}{c}\frac{dH(t)}{dt} \tag{2.4}$$

where $H(t)$ is the heating function of the laser pulse and can be approximated as a delta function. Equation 2.4 is usually solved by applying a Green's function, and the detailed solution can be found in [40].

When a spherical absorber of radius *R* and uniform optical absorption coefficient μ_a is excited by a laser pulse, the resultant PA wave has a N-shaped waveform [41]. Figure 2.1 shows the resultant pressure wave in the 1D case. The width of the N-shaped wave in temporal domain is equal to twice the quotient of *R/c*, where *c* is the speed of sound in the sphere.

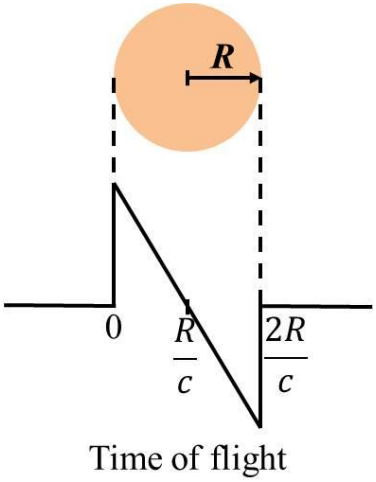

Figure 2.1: Pressure wave generated from a spherical absorber of radius *R* and speed of sound *c*.

Three crucial pieces of information can be obtained from the N-shaped wave generated from the source. Firstly, the amount of time between the firing of the laser and the detection of the wave represents the distance of separation between the source and the detector. Secondly, the physical size of the absorber can be measured by examining the

time difference between the two edges of the N-shaped wave. Lastly, the amplitude of the arriving PA wave can be used to quantitatively extract information on the optical absorption property of the absorber according to Equation 2.3.

The N-shaped PA wave generated above can also be analyzed in the frequency domain. For an absorber of radius *R*, and speed of sound *c*, its frequency amplitude spectrum $p(\omega)$ can be calculated according to [42]:

$$\boldsymbol{p(\omega)} = \frac{\left(\frac{\omega R}{c}\right)\cos\left(\frac{\omega R}{c}\right) - \sin\left(\frac{\omega R}{c}\right)}{\left(\frac{\omega R}{c}\right)^2} \tag{2.5}$$

The spectrum magnitude of two spherical absorbers with different sizes is shown in Figure 2.2. As the diagram illustrates, for PA imaging where a nanosecond excitation laser pulse is used to generate the PA wave, the resulting frequency content can extend possibly to hundreds of megahertz depending on the dimension of the absorber. Typically, smaller the absorber size, broader the bandwidth becomes. However, not all of the generated frequency content can be detected due to the finite detection bandwidth of the transducer.

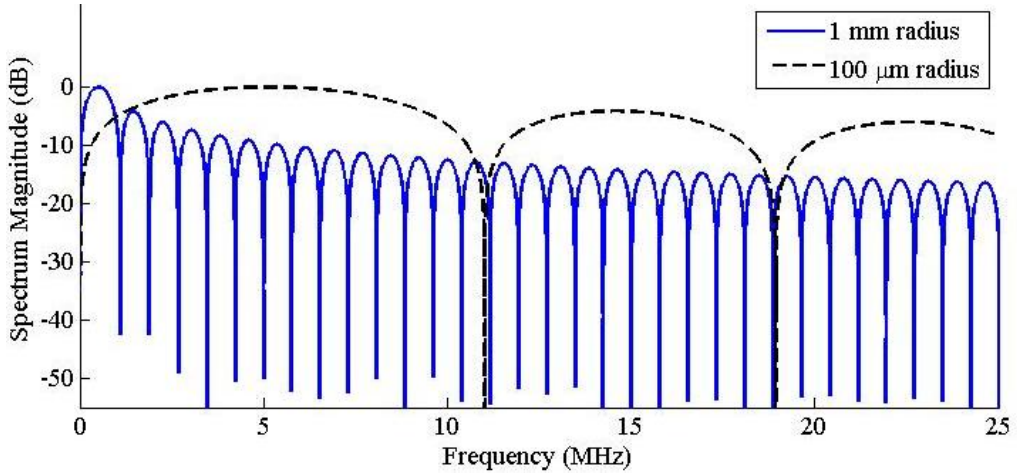

Figure 2.2: Frequency spectrum of two spherical absorbers of radius 1 mm and 100 μm.

2.4 Photoacoustic wave attenuation

There are several factors that can affect image quality, where signal attenuation often plays a key role. Its effect on the image quality is especially apparent in optical imaging. An optical imaging modality often has to make a compromise between either large imaging depth or high imaging resolution because of high photon attenuation in biological tissue. Transport mean free path (TMFP) describes the average distance a photon can travel before being attenuated. It is a parameter used to establish two regimes which a photon propagating through tissue can be in. Any photons that are collected within the TMFP are considered in the ballistic or quasi-ballistic regime. Otherwise, they are considered in the diffusive regime [43]. In order to achieve high spatial resolution, only ballistic or quasi-ballistic photons can be used. Optical imaging systems using such photons are generally referred to as ballistic imaging system. Considering that the average TMFP in soft tissue with a near-infrared light source is at most 1 mm, ballistic imaging modalities such as confocal microscopy or multiphoton microscopy have very limited imaging depth in order to achieve high spatial resolution of a few micrometers [44–46]. Such shallow imaging depth severely restricts the clinical applicability of the imaging technique [47]. Conversely, diffuse optical imaging uses photons in the diffusive regime. Modalities such as diffuse optical tomography are no longer limited by the TMFP and can penetrate several centimeters into tissue in near-infrared. The trade-off is their poor resolution typically in the millimeter range [47].

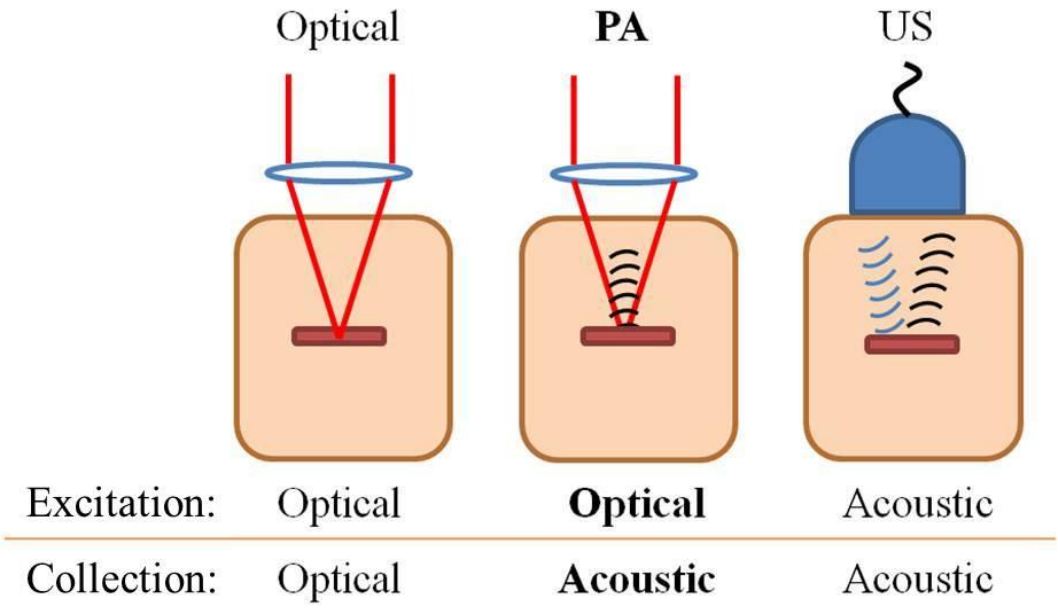

Figure 2.3: Illustration comparing three modalities: optical, PA, and US. Photons in optical modalities are attenuated optically twice, whereas they are only attenuated once in PA before being converted to acoustic wave, which is attenuated less in tissue.

The inherent bi-modal nature of PA imaging allows it to overcome the diffusion limited imaging depth faced by optical systems without sacrificing spatial resolution. As discussed in the previous section, unlike other optical systems, optical information in a PA system is transported by acoustic waves over a broadband of frequency. As Figure 2.3 illustrates, photons are attenuated only in the excitation path before conversion to acoustic waves through the PA effect. On the other hand, information obtained in other optical modalities undergoes optical attenuation twice in both the excitation and collection paths. The acoustic attenuation in tissue is frequency dependent and is estimated to be 0.6 dB $cm^{-1}MHz^{-1}$ [48]. The lower frequency PA signal is attenuated several orders of magnitude less than the optical counterpart [49]. The higher frequency signal over ~15 MHz is still attenuated quickly in tissue. Considering the fact that an US

transducer has limited detection bandwidth, the higher frequency signal is not detected regardless of the attenuation. Therefore, PA imaging is capable of imaging deeper than common optical modalities.

2.5 Photoacoustic contrast mechanism

As shown in Equation 2.3, PA imaging contrast originates from the mechanical (β, c), thermodynamic (C_p), and optical (μ_a) properties of tissue. The Grueneisen parameter expresses the first three parameters as a single entity, and it describes the thermo-mechanical property of the tissue. The optical absorption coefficient is the dominating source of PA imaging contrast in biological tissue since it can vary several orders of magnitude among various tissue constituents. The Grueneisen parameter, however, has much lower variation in soft tissue. PA imaging is thus often referred to as an absorption based modality.

Figure 2.4 shows the optical absorption coefficient of the main absorbers in biological tissue. Below 1000 nm, both oxy-haemoglobin (HbO_2) and deoxy-haemoglobin (HHb) are the most absorbing tissue constituents, with several orders of magnitudes higher absorption than water or lipid. This allows high contrast PA imaging of the vasculature [2]. The spectra differences between HHb and HbO_2 can be used for measuring haemoglobin concentration and blood oxygenation level [50]. Although melanin has higher absorption than haemoglobin, the melanin distribution is considered to be highly localized to the skin and retina, where blood is a major tissue constituent

throughout the body [51,52]. Above the 1000 nm regime, both water and lipid start to dominate over hemoglobin in optical absorption.

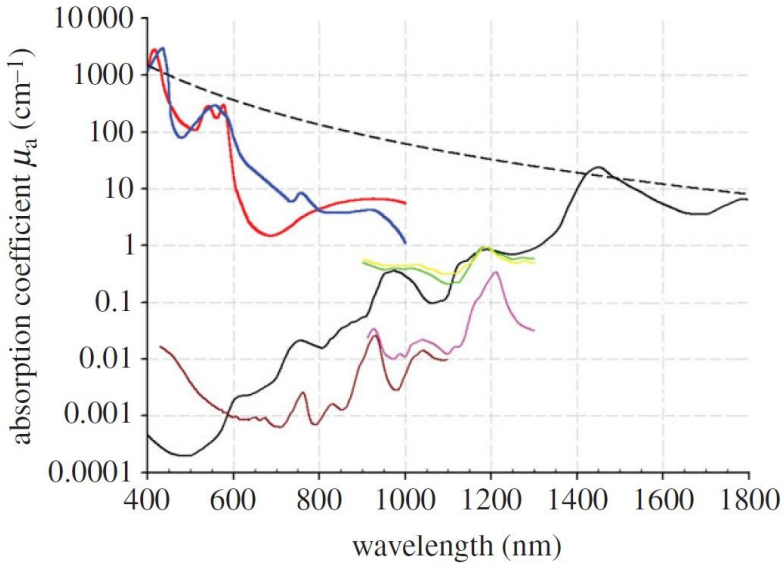

Figure 2.4: Optical absorption coefficient, $\boldsymbol{\mu_a}$, of various tissue chromophores. Black dash line: melanin; Red line: oxy-haemoglobin (HbO_2); blue line: deoxy-haemoglobin (HHb); black solid line: water; yellow line: elastin; green line: collagen; pink and brow lines: lipid [21].

Chapter 3: Photoacoustic Imaging System

In this chapter, an overview of our PA imaging system is presented. The system is a type of the limited-view PAT configuration where the laser illuminates a large tissue area, and a commercial linear array US transducer is used as the detector. Specific information regarding each part of the setup is detailed below. Optimization and improvement made to the synchronization and acquisition scheme are also presented. The back-projection algorithm used in reconstruction of PA images from the received raw data is described. Finally, imaging phantoms are tested for characterizing the system performance.

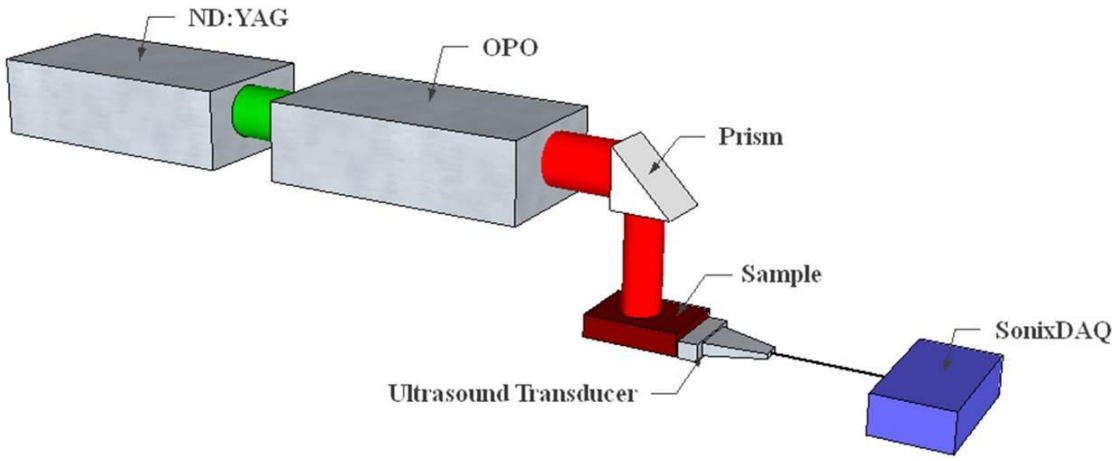

Figure 3.1 The schematic of the essential pieces in the PA imaging system. ND:YAG: Surelite II neodymium-doped yttrium aluminum garnet laser; OPO: optical parametric oscillator.

3.1 Light source

As mentioned in Chapter 2, the illumination light plays a key role in PA imaging. Its pulse width needs to be sufficiently short to successfully induce the PA effect, and its wavelength determines which constituent of the tissue is the dominating source of

imaging contrast. The ability to tune the laser to a specific wavelength depending on the application is vital for the system to image various types of absorbers.

A Surelite II laser coupled with an optical parametric oscillator (OPO), both manufactured by Continuum, Inc. (Santa Clara, CA, USA), is used as the light source. Surelite II is a Q-switched pulsed neodymium-doped yttrium aluminum garnet (ND:YAG) laser. The laser outputs 532 nm light at 10 Hz repetition rate with peak energy of 350 mJ. The pulsewidth is 5 ns. The peak energy is adjustable for possible clinical applications where the illumination energy is required to meet the ANSI safety limit. The 532 nm light from the Surelite II laser then pumps an OPO unit for wavelength tuning. The OPO is a passive unit capable of converting the incoming pump light of frequency ω_p into two outgoing waves known as the signal and the idler of frequencies ω_s and ω_i respectively through nonlinear optical interaction [53]. The sum of the frequencies of the two output waves equals to the input wave frequency:

$$\boldsymbol{\omega_p = \omega_s + \omega_i} \tag{3.1}$$

By utilizing either the signal or the idler output, we can tune the output wavelength from 680 nm to 2500 nm. Shorter wavelength such as 700 nm is typically used for imaging blood-rich tissue such as porcine liver, and longer wavelengths of 930 nm or 1210 nm are chosen for fatty tissue due to the high absorption peaks of lipid at those wavelengths as shown in Figure 2.4. The OPO peak output energy is wavelength dependent and can reach as high as 120 mJ at around 700 nm. Given a typical illumination area of ~3 cm^2, this energy translates to a fluence rate, *F*, of 40 mJ/cm^2. Table 3.1 summarizes the laser specifications.

Table 3.1: Specifications of the pump laser source and the optical parametric oscillator

Laser Specifications		
Pump laser source	Type	ND:YAG
	Repetition rate	10 Hz
	Center wavelength	532 nm
	Output energy	350 mJ
Optical parametric oscillator (OPO)	Tunable wavelength range	680 – 2500 nm
	Peak output energy	120 mJ
	Pulse width	5 ns

3.2 Photoacoustic wave detection

A commercially available 38mm wide 128-element linear-array ultrasound transducer (Model: L14-5/38mm) is used as the PA wave receiver. The center frequency of the transducer is 7.2 MHz with 70% fractional bandwidth. Since a typical PA wave is considered to be broadband, the US transducer effectively acts as a band-pass filter, discarding frequency content outside of the bandwidth. In clinical applications which require up to several cm of imaging depth, the high frequency PA signal is already attenuated acoustically before reaching the US transducer. The received data is then acquired through a module called the SonixDAQ (Ultrasonix Medical Corporation, BC, Canada). It is a specialized research module developed for receiving raw acoustic data simultaneously from all 128 channels at 40 MHz sampling rate. The stored raw data is uploaded to a Windows based US unit (SonixMDP, Ultrasonix Medical Corporation) via a USB 2.0 interface. The SonixMDP is also responsible for hardware initialization and running acquisition software as well as tuning the output wavelength of the laser system through a RS-232 connection.

3.3 Synchronization and acquisition

For an imaging system that consists of separate transmission and receiving units such as ours, accurate synchronization plays a key role in the data acquisition process. It is also the main aspect in the system setup where several designs are investigated for optimization and improvement.

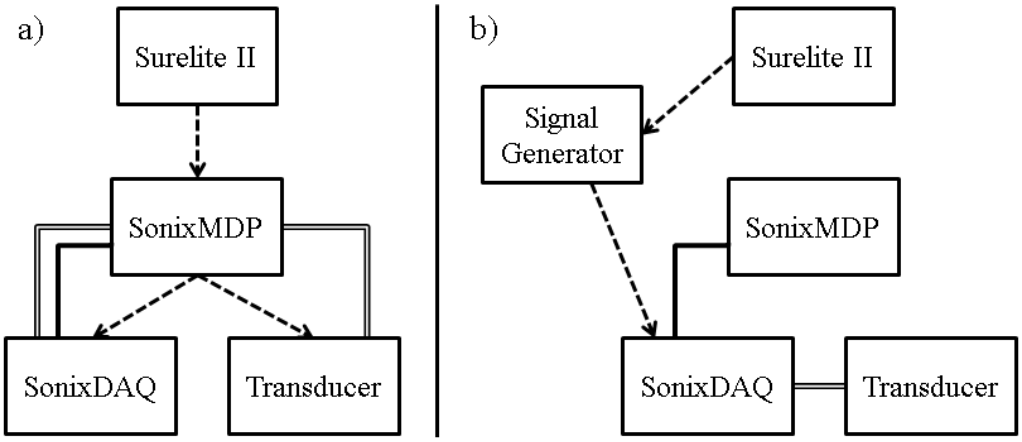

Figure 3.2: Two synchronization trigger signal setups. Dashed lines: trigger signal pathway; double solid lines: DL1-156 zero insertion force (ZIF) connector; single solid line: USB 2.0 connection. a) the original setup where the Surelite II triggers the SonixMDP which in turn triggers both the SonixDAQ and the transducer; b) trigger signal from Surelite II is inverted through a signal generator which in turn triggers the SonixDAQ directly. Note that SonixMDP acts as a bridge in transferring received data from the transducer to the SonixDAQ in (a), and in (b) a specialized connector is used instead.

In the first design, data acquisition is synchronized to the laser source (Figure 3.2(a)). A trigger signal generated from Surelite II upon each laser pulse is first passed into the SonixMDP. A trigger signal relayed from the SonixMDP then activates the SonixDAQ to start data acquisition for one frame. Each subsequent firing of the laser pulse results in an additional frame to be stored inside the SonixDAQ until a user set

buffer size is filled. Finally the entire set of frames is uploaded via USB 2.0 to the SonixMDP. Two major problems, however, arise from this design.

First of all, the start of frame acquisition by the SonixDAQ, t_{DAQ}, lags behind t_{pulse}, the time each laser pulse is fired at the sample, as shown in Figure 3.3. The time difference is found to be approximately 15 μs. Since the PA wave is being generated precisely at t_{pulse}, such a lag restricts how close the sample can be to the surface of the transducer. Moreover, in order to reconstruct the image successfully, the beginning of each frame needs to be padded with the correct amount of zeroes to compensate for the lag. The cause of such delay is determined to be of two origins: shape of the trigger signal and inherent hardware and software delay within the SonixDAQ. The output trigger signal from Surelite II is an inverse square wave of duration ~12 μs. While the falling edge of the triggering square wave corresponds to t_{pulse}, SonixDAQ is designed to be triggered on the rising edge. In addition, there are several μs of lag caused by both the hardware and the data acquisition software of the SonixDAQ.

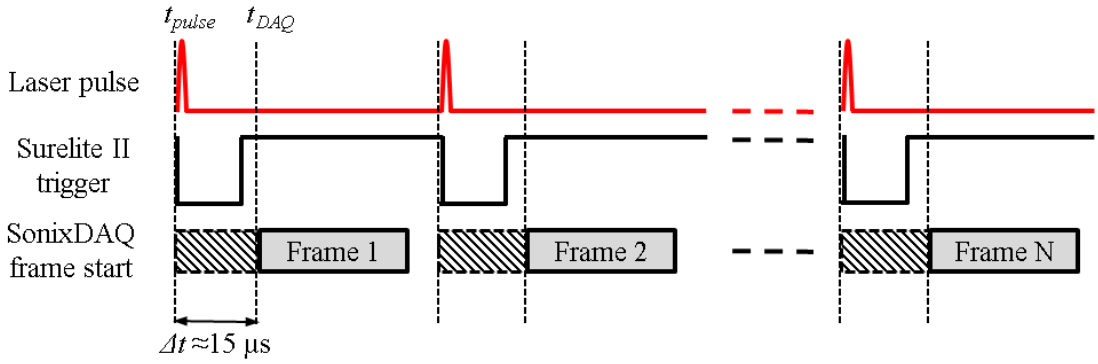

Figure 3.3: Trigger signals and frame acquisition timeline. The start of each frame did not coincide with each laser pulse. Samples within the first 15 μs cannot be measured. Not drawn to scale.

The second problem is related to data acquisition. As shown in Figure 3.2 (a), the SonixMDP acts as a bridge between SonixDAQ and the US transducer. Received data from the transducer passes through SonixMDP first before being amplified and stored into the onboard buffer in the SonixDAQ. This introduces a large amount of electronic noise to the raw data as shown in Figure 3.4 (a). A low-pass filtering with cutoff frequency at 15 MHz is implemented to remove most of the noise while some vertical noise artifacts remain unfiltered.

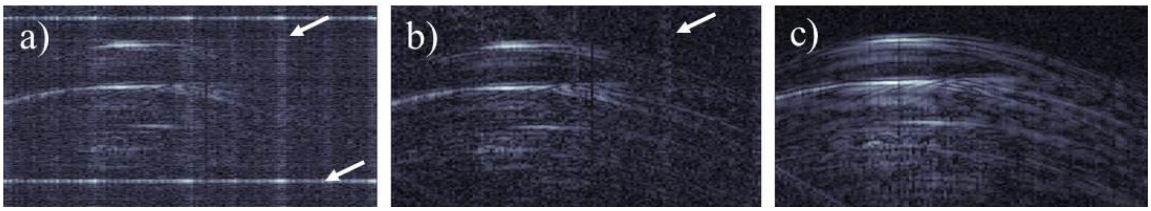

Figure 3.4: Comparing raw SonixDAQ received data. a) original setup without filtering; b) original setup with low-pass filtering; and c) improved setup without filtering. Arrows denote the vertical and horizontal pattern noise artifact. Each image is approximately 2×4 cm.

To solve both the above mentioned problems, a revised design is implemented (Figure 3.2 (b)). There are two major changes in the second design. Firstly, a specialized connector manufactured by Ultrasonix allows the US transducer to make a direct connection to SonixDAQ, bypassing the SonixMDP. This essentially reduces the role of the SonixMDP to only storing data in memory. The raw data received in this fashion is shown in Figure 3.4 (c). It should be noted that this set of data is displayed without any filtering. Not only is the noise reduced, more details are also preserved since low-pass filtering is not required. There is, however, one major drawback to this design. With the transducer being directly connected to a passive data receiving module, it can no longer actively transmit any US pulses. It does not affect PA imaging since the transmission is

generated from the laser and the transmitting mode has to be turned off to avoid interference with the PA wave. This will be problematic when both US B-mode imaging and PA imaging are required to be performed with the same setup. In this case, the transducer has to be able to both transmit and receive and therefore it needs be connected to the SonixMDP similar to the first design. Since the frame rate of PA imaging is limited by the repetition rate of the laser pulse at 10 Hz, the US B-mode imaging can be acquired between two laser pulses. Another change in the design is the direct triggering of the SonixDAQ by Surelite II. A signal generator is placed between the two for inverting the square wave generated by the laser. Such a trigger pattern, however, does not fully reduce the time lag to zero between the laser and the SonixDAQ. There are still approximately 5 μs of lag caused by both the hardware and software, which restricts the system in imaging samples close to the transducer.

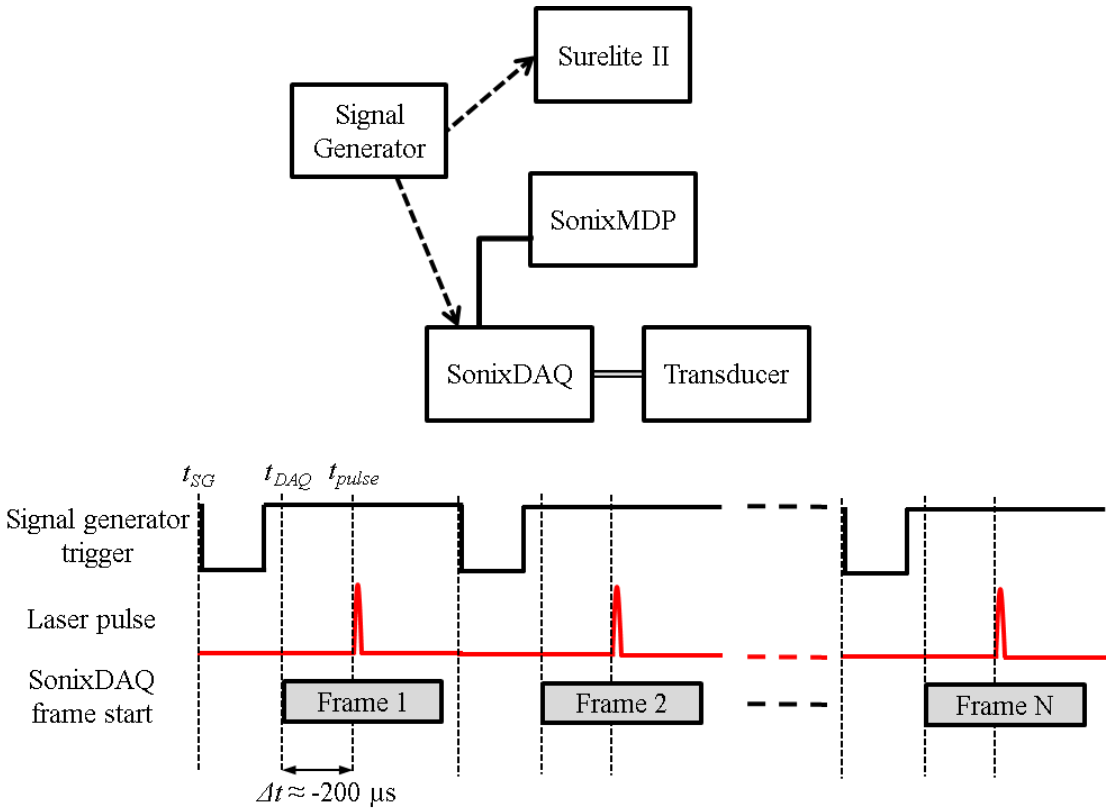

Figure 3.5: Top: the finalized synchronization and acquisition system setup. Bottom: the corresponding trigger signal and frame acquisition timeline. Not drawn to scale.

With help from Hamid Moradi, an additional optimization is made to the setup to resolve the time lag issue. As shown in Figure 3.5, in the third design, a signal generator is used as the trigger source that triggers both Surelite II for firing a laser pulse and SonixDAQ to start data acquisition. Similarly, the SonixDAQ is triggered on the rising edge and frame acquisition starts shortly thereafter. As shown in Figure 3.5, the only difference is that t_{pulse} now takes place ~200 µs after t_{DAQ}. This is due to the operating nature of the Q-switched laser unit. In short, the external trigger sent to the laser only triggers the flash lamp, a process within the laser cavity that builds up population inversion. Upon receiving a Q-switch trigger which is controlled internally by the laser,

the laser outputs a nanosecond high energy pulse [54]. The time delay between the flash lamp trigger and Q-switch trigger, usually several hundreds of μs, is called the Q-switch delay. This delay can be adjusted and it controls the output power of the laser. This delay has resulted in t_{DAQ} happening prior to t_{pulse}. By placing an accurate amount of delay in the acquisition software before each frame acquisition, one can synchronize t_{DAQ} and t_{pulse} properly. This delay time is determined experimentally to be 209 μs. For future implementation, two trigger signals can be used to trigger the laser, where the first signal triggers the flash lamp and the second one triggers the Q-switch. In this approach, the second signal can also trigger the SonixDAQ and synchronize t_{DAQ} more precisely with t_{pulse}.

3.4 Photoacoustic image reconstruction

The goal of image reconstruction in PA imaging is to obtain a map of the initial pressure distribution, p_0, generated by the PA effect, from the raw data acquired by the SonixDAQ. Retrieving p_0 is quite essential to PA imaging because it contains several important tissue parameters, most noticeably the absorption coefficient (Equation 2.3). Back-projection, k-space reconstruction, and the inverse Radon transform are a few of many reconstruction techniques developed for PA imaging [14,55,56]. In this project, back-projection is chosen as the reconstruction algorithm for its simplicity and versatility.

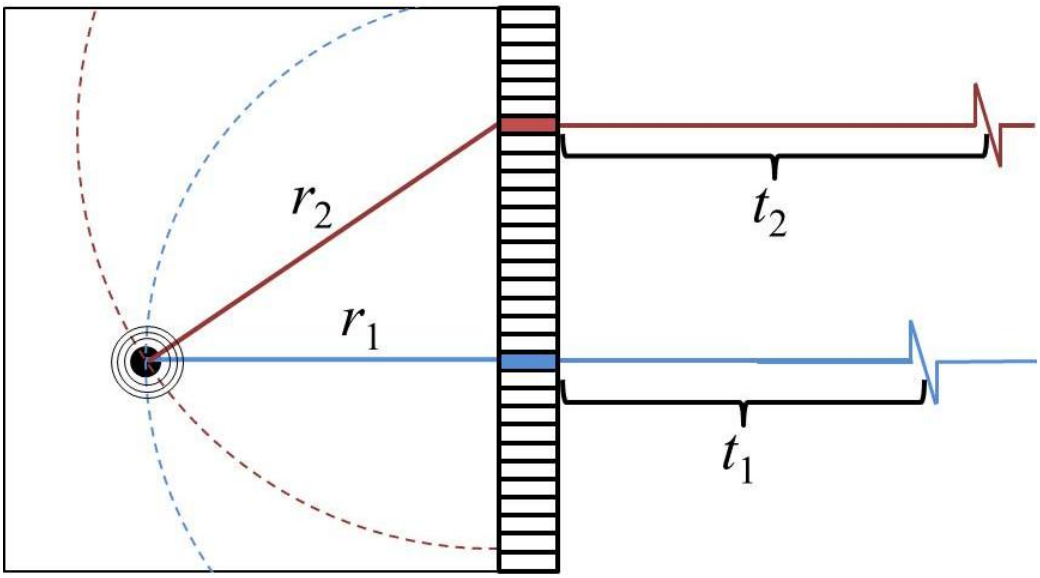

Figure 3.6: 2D illustration of the back-projection principle. The PA source, located r_n away from the n_{th} channel in a linear array transducer, generates a PA wave that is detected at time $t_n = r_n/c_m$, where c_m is the speed of sound of the medium.

When a PA wave is generated from a source, it propagates out toward the surface of the sample. When a transducer records a pressure wave at time t after the laser excitation, the physical distance between the transducer and the PA source, r, can be calculated by $r=tc_m$, where c_m is the speed of sound of the medium. As Figure 3.6 illustrates, the detected signal needs to be projected onto a circular arc of radius r to account for all possible locations the particular PA source might be at. The overlapping point of all the arcs produced by the transducer array indicates the location of the PA source.

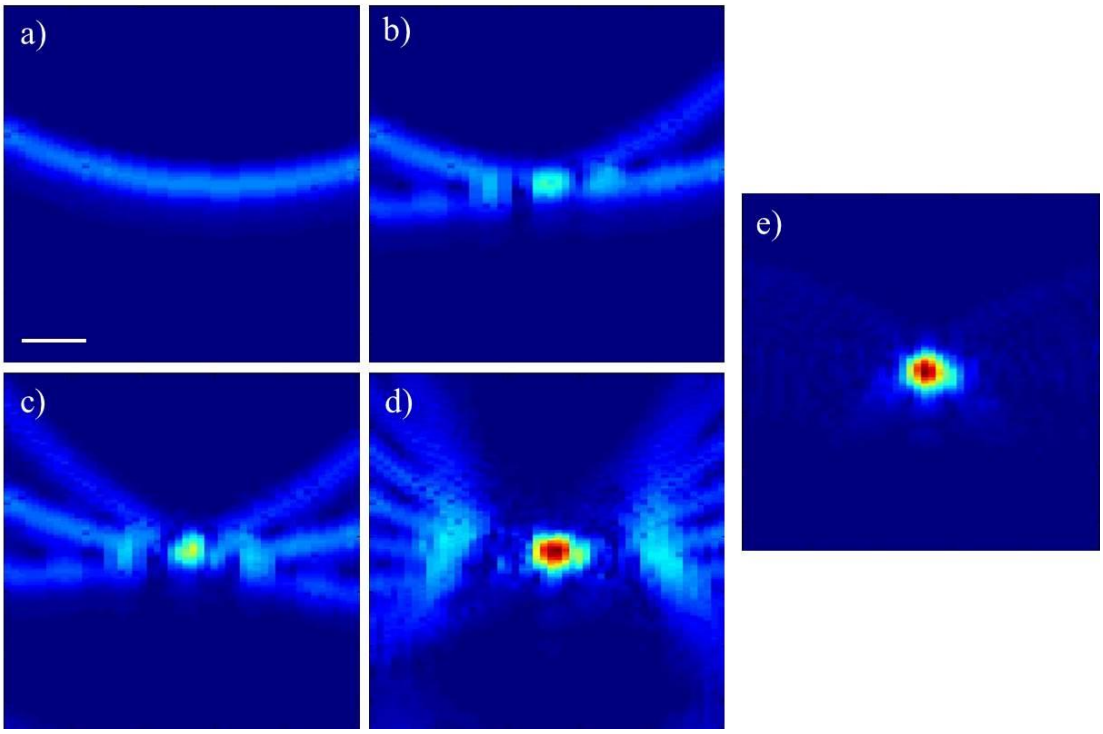

Figure 3.7: Reconstruction of a small point-source like object using (a) 1 channel, (b) 2 channels, (c) 3 channels, (d) 10 channels, and (e) 128 channels of the acquired data. Scale bar denotes 1mm.

In theory, only two transducers are needed to pinpoint a point source in 2D PA imaging. In practice, however, many more transducers are required for high quality image. Figure 3.7 compares the image reconstruction of a point-source like object when different numbers of transducers (selected from a 128 element linear array transducer) are used. Figure 3.7 (a) illustrates the reconstructed image if only the data received by one transducer is used. As we can see, only a single arc of signal is reconstructed with no possible information on where the source is located. Figure 3.7 (b) is the result of reconstruction from a pair of transducers. Although the point source can be vaguely identified at the overlapping point of the two arcs, it has extremely poor quality. Since the overlapping point is the sum of the two arcs, its signal intensity is only twice as much

as the arcs, equivalent of a 6dB signal-to-noise ratio (SNR). As more channels are used, the reconstructed image becomes more point-source like. One major improvement with using all 128 channels is the suppression of the reconstruction artifacts due to the back-projecting arcs. Mathematically, the intensity of the reconstructed point source with 128 channels of data is 42 dB stronger than the arcs, whereas it drops to 20 dB for the 10 channel case.

3.5 System characterization

To demonstrate and characterize the PA system, several phantoms are manufactured and the reconstructed images are analyzed in the following sections.

3.5.1 Axial and lateral resolution

A common method in determining spatial resolution is to measure the full-width-half-maximum (FWHM) of the point-spread-function (PSF). For PSF measurement, an object with spatial dimensions much smaller than the system resolution is typically used. For PA imaging, one approach is to focus the excitation light onto a piece of black foil in order to generate a point-source image [18]. A different approach by imaging the cross-section of a single strand of human hair embedded in gelatin phantom is chosen in our study as shown in Figure 3.8. The average diameter of a human hair strand is ~70 microns which is well below the theoretical resolution of our system according to Equation 3.2 [57].

The result is shown in Figure 3.9 with the axial and lateral profile through the maximum peak plotted in scale on the side. The image can be regarded as a close approximation to the PSF of our system. The FWHM values, which correspond to the spatial resolutions, are determined to be 0.44 mm and 0.52 mm for axial and lateral directions respectively.

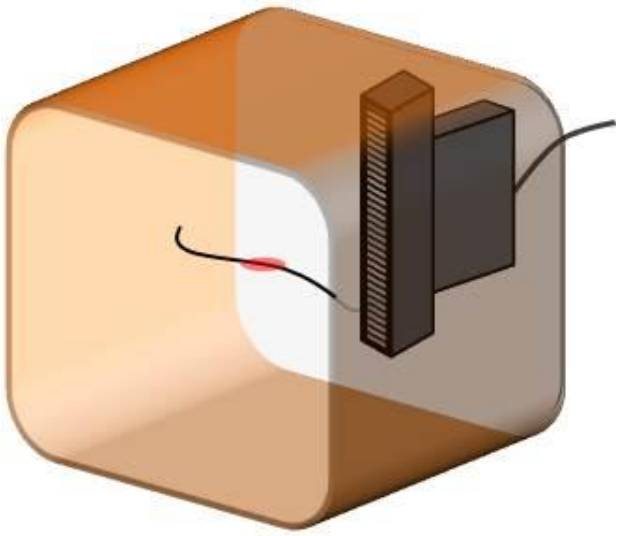

Figure 3.8: Setup used to image the cross-section of a hair strand. The red disk represents the illumination area. Not drawn to scale.

In conventional pulse-echo US imaging, axial resolution is determined by half the spatial pulse length, which is defined as the product of the number of cycles in a pulse and its wavelength [58]. This is why a high frequency US transducer (i.e. center frequency of 50 MHz) can resolve objects in the order of several tens of microns since it can transmit pulses with much shorter wavelength. Ultimately, the resolution in US imaging depends on the frequency content of the received signals. Similarly, axial resolution in PA imaging is also a function of the frequency spectrum of the received

signal. When a band-limited transducer is used, the higher cut off frequency (f_{cutoff}) of the transducer determines the axial resolution.

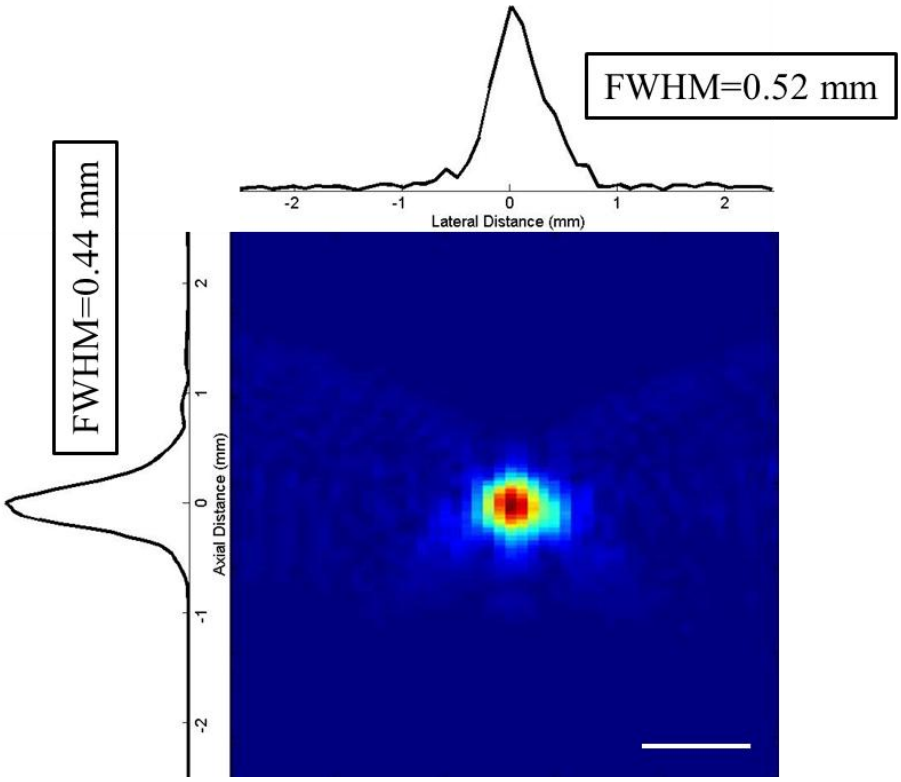

Figure 3.9: The reconstructed PA image of the cross-section of a hair strand. The axial FWHM distance is 0.44 mm, and lateral FWHM is 0.52 mm. Scale bar denotes 1 mm.

Equation 3.2 describes the theoretical PSF of PA imaging with a limited bandwidth US detector [59]:

$$\boldsymbol{I(R)} = \frac{\boldsymbol{K^3}}{\boldsymbol{2\pi^2}}\left[\frac{\boldsymbol{J_1(KR)}}{\boldsymbol{KR}}\right] \tag{3.2}$$

where $K = 2\pi f_{cutoff}/c$, R is the displacement from the point source, and $J_1()$ is the first-order spherical Bessel function of the first kind. For example, the transducer used in our system has a higher cut off frequency (f_{cutoff}) at 14 MHz. The theoretical axial resolution can be estimated from Eq. 3.2, and it is 0.10 mm for our transducer. There are

several factors that may have affected the degraded axial resolution obtained in the previous experiment. First of all, Equation 3.2 assumes the US transducer is a point detector that has an ideal flat frequency response in the bandwidth. In practice, a transducer has finite dimension and a frequency response that resembles a Gaussian shape. Second, it assumes that the detected PA signal propagates through a lossless medium. This cannot hold true in reality, as any medium will attenuate the acoustic signal to a certain degree. As mentioned earlier, higher frequency signals are attenuated more quickly than the lower ones, effectively altering the frequency content of the received signal. Lastly, the received signal is convoluted with the electrical impulse response of the transducer which further degrades the resolution.

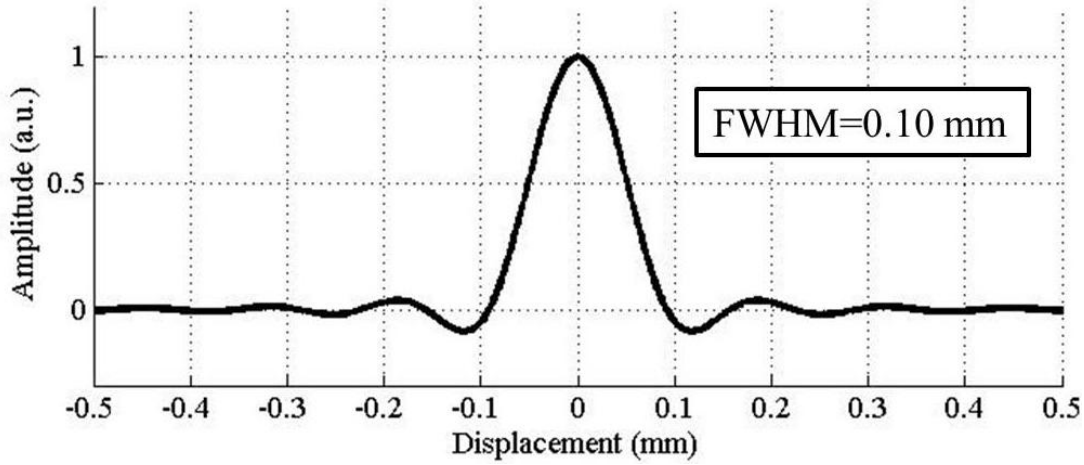

Figure 3.10: Theoretical PSF for a transducer with a high cut off frequency of 14 MHz. The FWHM is 0.10 mm.

3.5.2 Field of view

In the imaging plane, the field of view (FOV) is limited by the spot size of the excitation light. Since NIR wavelengths are often used, visual measurement of the spot size is rather difficult and inaccurate. A method is devised to obtain a quantitative

measurement of spot size by imaging an array of black dots printed onto a piece of paper (Figure 3.11). Each dot is approximately 0.1 mm in diameter and spaced 1 mm apart.

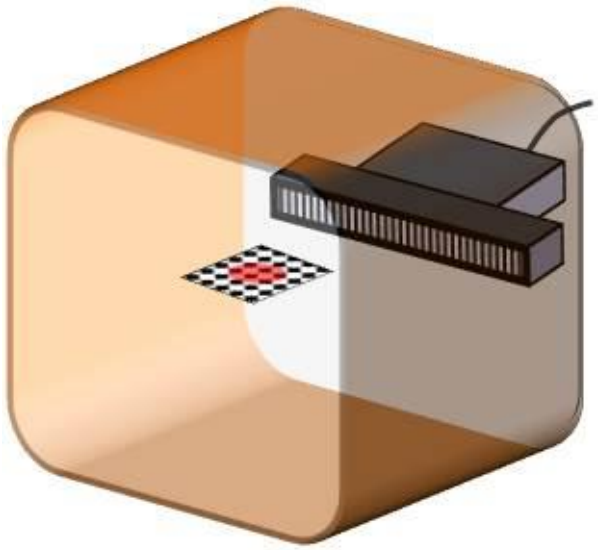

Figure 3.11: Setup used to image the arrays of dots printed on a piece of paper. The red disk represents the illumination area. Not drawn to scale.

Figure 3.12 displays the reconstructed PA images of the same dot array pattern under three different laser wavelengths. A circle of 20 mm diameter is drawn on each figure for visual reference. It is observed that the PA intensity does not have a smooth Gaussian distribution. This can be caused by the non-Gaussian distribution of the laser beam. Another reason is that the printed dots may have uneven shades of black, resulting in varying amount of absorption for each dot. Also, the misalignment of the paper phantom within the image plane of the transducer may also affect the distribution of the PA intensity.

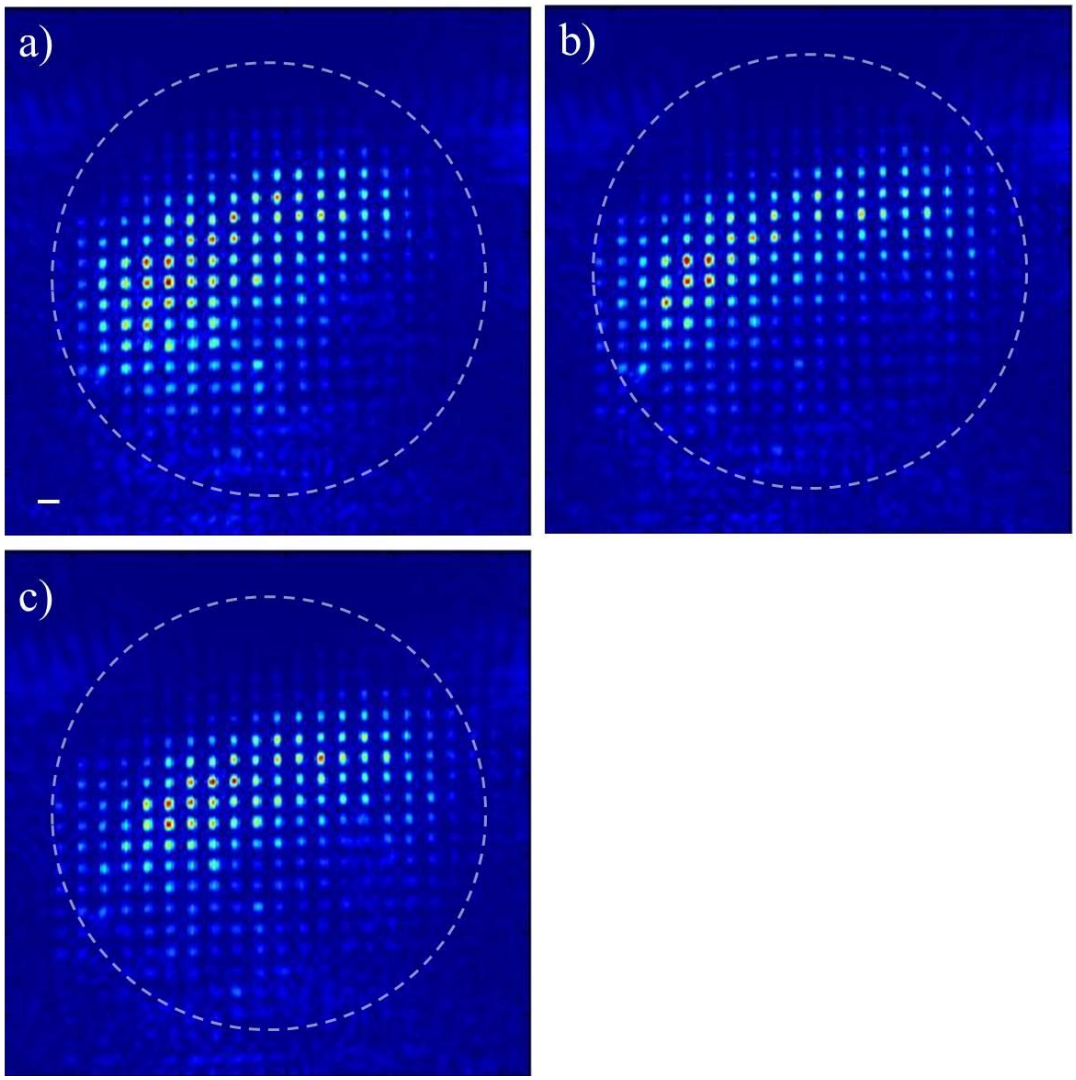

Figure 3.12: PA images of printed dot arrays with (a) 700 nm, (b) 800 nm, and (c) 900 nm excitation wavelength. Dashed circles of 20 mm in diameter are shown for reference. Scale bar in (a) denotes 1 mm.

From Fig. 3.12, an effective FOV is found to be ~3 cm^2 circular area in this PA system. The FOV can be increased by expanding the laser beam but eventually it is limited by the laser fluence that are required to excited PA signal. In tissue imaging, the incident light is quickly scattered and diffused before reaching the desired imaging depth, resulting in a more uniform distribution of energy. An optical diffuser can also be used to

improve the uniformity of the laser energy distribution, removing any hot-spots in the energy distribution.

3.5.3 Limited-view PAT limitation

In this section, an important limitation of limited-view PAT configuration such as ours is presented. As Figure 3.13 illustrates, when imaging samples with structures that are perpendicular to the transducer surface, it becomes extremely difficult for PA imaging to detect such structures. The reason lies within the directionality of the PA wave. For a single point source, the generated PA wave is spherical. The PA wave generated from a line source, however, exhibits a clear horizontal wavefront that propagates away from the line source. If the transducer is placed perpendicularly to the line structure, it cannot receive the PA wave that propagates in the perpendicular direction. For circles, it becomes increasingly difficult to identify the arc as the tangential line to the arc approaches 90^{o} relative to the transducer, whereas for a square pattern, there are nearly no signals received from the two vertical sides. In order to detect the missing structures, the transducer needs to be rotated to acquire PA signals from additional angles. In most *in-vivo* applications such as prostate imaging, however, multi-angle access is difficult. Paltauf et al. has proposed an iterative reconstruction method in order to compensate for lack of information in limited-view PAT [29].

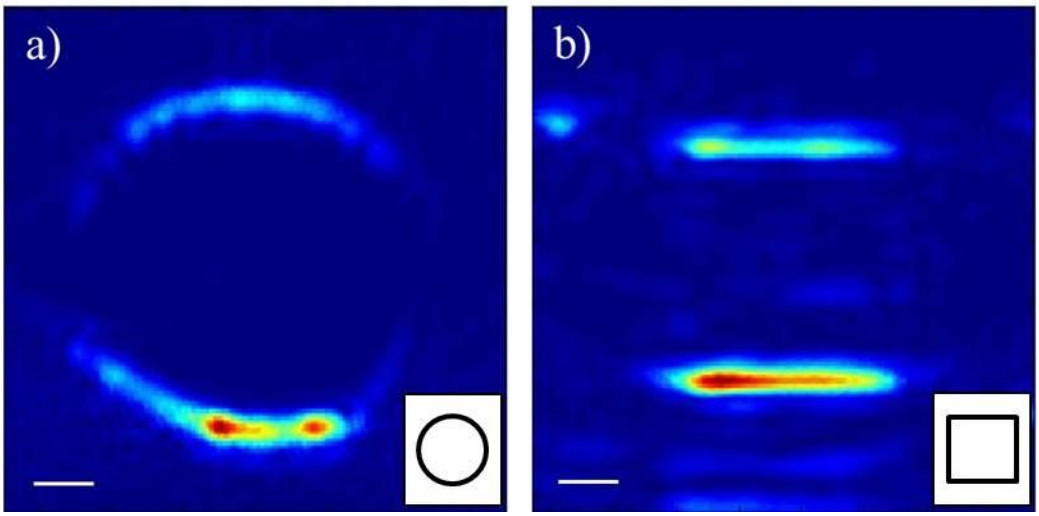

Figure 3.13: PA image of (a) a printed circle pattern and (b) a printed square pattern. The original printed patterns are shown in the insets.

Chapter 4: Photoacoustic Imaging of Brachytherapy Seeds

Prostate cancer is the leading incident cancer in the male population in developed countries [60]. Amongst the 100,000 newly reported cancer cases in Canadian men in 2013, nearly a quarter of the cases were prostate cancer [61]. Since the introduction of prostate specific antigen (PSA) screening in the early 1990s, many cases of prostate cancer can be detected at an early-stage and a wide range of treatment options have become available for patients such as radical prostatectomy, brachytherapy, external beam radiotherapy and primary androgen deprivation therapy [62]. Brachytherapy is emerging as the second most popular form of therapy following radical prostatectomy for low-risk localized prostate cancer patients [63].

Brachytherapy involves the implantation of radioactive sources known as seeds directly into the cancerous tissue region. These seeds are small cylindrical metallic casings with radioactive sources of either iodine-125 or palladium-103. In comparison to radical prostatectomy, brachytherapy can be performed on an outpatient basis with short recovery time and less severe side-effects [22]. Figure 4.1 illustrates a typical prostate brachytherapy procedure. The specialized US probe inserted into the rectum is the TRUS probe.

As mentioned in Chapter 1.3, accurate placement of the seeds is essential and TRUS imaging enables the physician to monitor the inserted seeds in real-time and make necessary adjustments. Studies have shown, however, that TRUS imaging can sometimes suffer in imaging quality on visualizing brachytherapy seeds due to their small size (the diameter is approximately three times the acoustic wavelength), speckle, acoustic

shadowing, and off-axis seed orientation [64]. An alternative method is to include X-ray fluoroscopy as a secondary modality to depict the distribution of seeds in addition to TRUS. X-ray, however, exposes both patients and clinicians to additional radiation, and imaging cannot be performed simultaneously with TRUS, rendering the procedure more time-consuming. Therefore, various attempts have been made to improve seed localization using ultrasound based techniques such as magnetically induced motion imaging [65], transurethral ultrasound imaging [66], and 3D TRUS imaging [23].

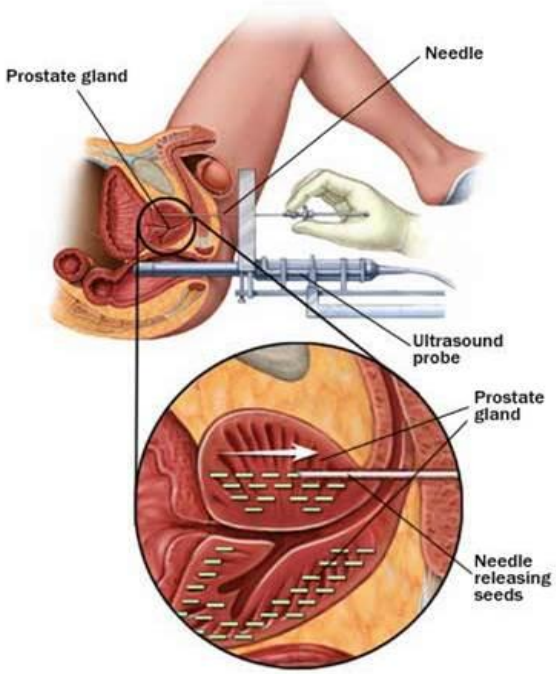

Figure 4.1: Drawing of a prostate brachytherapy procedure. Radiating seeds are inserted using brachytherapy needles, while the TRUS probe continuously monitors the seeds location. © Mayo Foundation for Medical Education and Research. All rights reserved. (http://www.mayoclinic.org/tests-procedures/prostate-brachytherapy/multimedia/permanent-prostate-brachytherapy/img-20008710)

PA imaging is shown to be a strong candidate for brachytherapy seed imaging due to its absorption-based imaging principle [5,25]. As Figure 4.2 illustrates, stainless

steel, a commonly used material in brachytherapy seeds, has high absorption. The challenge, as stated earlier, is the limited imaging depth due to high optical attenuation in tissue. In this chapter, as initial feasibility tests, we present the methods applied to modify brachytherapy seeds in order to increase its PA contrast. The difference in performance between the modified seeds and non-modified seeds are compared.

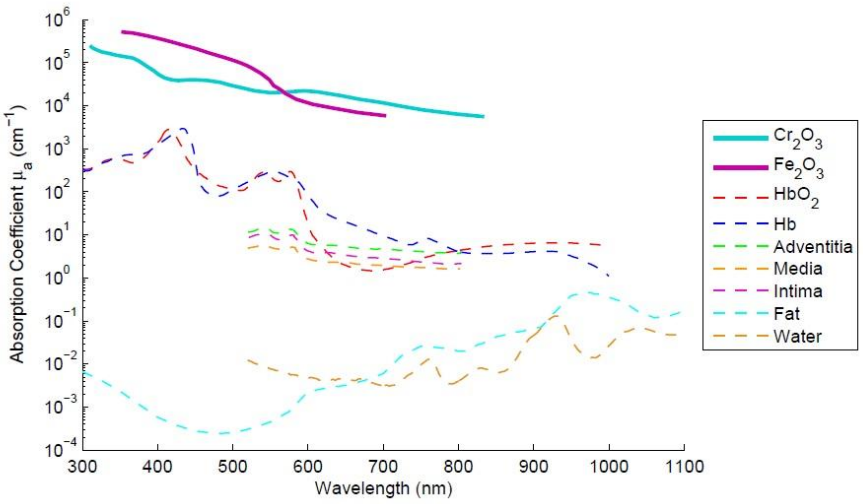

Figure 4.2 Absorption spectra of the major tissue constituents with the addition of Cr_2O_3, a common surface passivation layer of stainless steel, and Fe_2O_3, the core of stainless steel [25].

4.1 Methods

Figure 4.3 shows the PA imaging set up. As detailed in Chapter 3.3, triggering is initiated by the laser source and relayed directly to SonixDAQ. The US imaging plane is adjusted to align with the seeds and held in stationary position throughout the experiment.

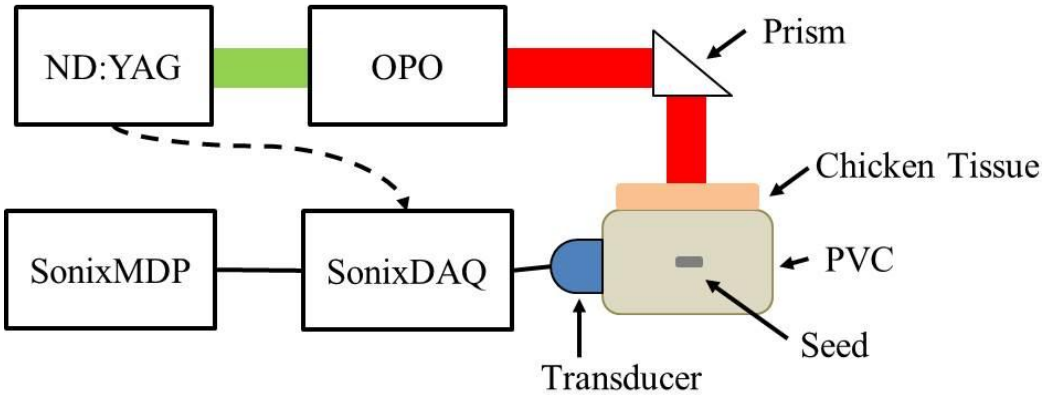

Figure 4.3: Setup diagram of the PA system used. Layers of chicken tissue were varied to simulate different optical penetration depth. Dashed line represents that the laser unit is triggering the SonixDAQ directly.

Non-radiating brachytherapy seeds (OncoSeed Model 6711), 4.5 mm in length and 0.5 mm in diameter, from Oncura, Inc. (Arlington Heights, IL, USA) were used (Figure 4.4). Two different methods of seed modification were investigated. In the first method, a layer of black paint was used as an absorption enhancing material and applied as coating to the seeds. To study the effect of the coating, the coated seed was inserted into a polyvinyl chloride (PVC) phantom along with a bare seed and imaged under different wavelengths to obtain the PA spectrum of the seeds. Experiments comparing the imaging depth of the coated and the bare seeds were also performed. Lastly, a gelatine phantom was prepared to embed three pairs of coated and bare seeds for multiple-seed imaging. For the second method of modification, a layer of silver was chemically deposited on the seed through reduction reaction. A similar experiment was performed to characterize the enhancement effect from the silver coating.

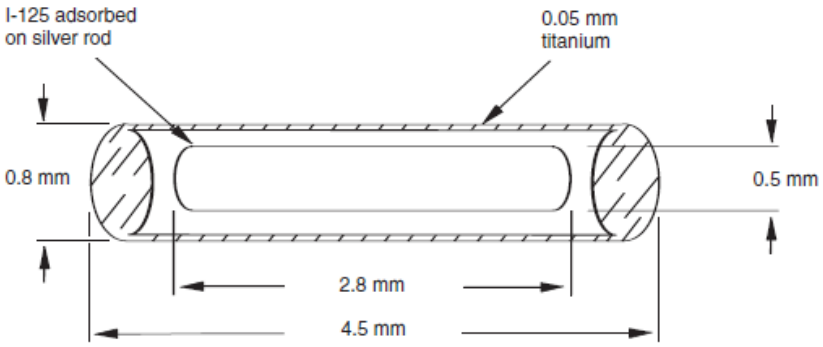

Figure 4.4: Schematic drawing of a brachytherapy seed.

4.2 Results

4.2.1 Black paint coated seed

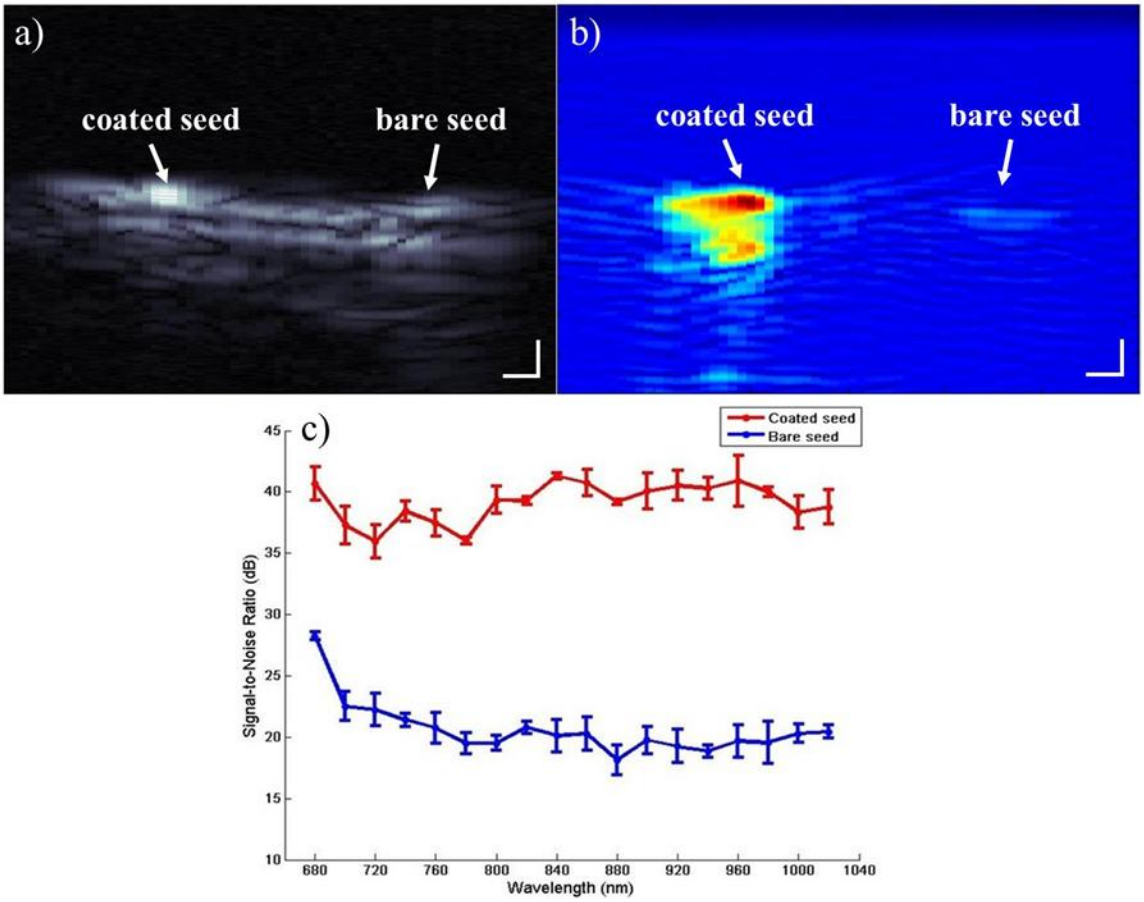

Figure 4.5: (a) B-mode and (b) PA imaging at 680 nm wavelength of the PVC phantom containing a coated seed and a bare seed. Horizontal and vertical scale bars denote 2 mm. (c) SNR of both coated and bare seeds from 680 nm to 1020 nm, representing the PA spectrum. Error bars denote the standard deviation of averaging 10 frames at each wavelength.

One coated seed and one bare seed separated by 9 mm are inserted via a brachytherapy needle into a PVC phantom. Figure 4.5 (a) and (b) shows the B-mode image and the corresponding PA image at 680 nm excitation wavelength of the PVC phantom containing the coated and the bare seed. The seed detection in the B-mode image is poor mainly due to the air gap created by pulling out the brachytherapy needle

used to implant the seeds in the phantom. The same air gap does not pose problems in PA imaging since air does not generate any PA signal. In order to obtain the PA spectrum of the seeds, the excitation wavelength of the laser is tuned from 680 nm to 1020 nm in 20 nm steps. Figure 4.5 (c) shows the resulting signal-to-noise ratio (SNR) in decibels of the PA spectrum of the two seeds. A 5 mm by 1mm region-of-interest (ROI) is manually centered at each seed location, from which the brightest 1 % of the pixels are used to calculate the signal intensity of each seed. The noise level is calculated from the background. The same technique is used to calculate the SNR for the other images in this chapter. It is clear that the coated seed outperformed the bare seed over the entire scanned wavelengths with a mean increase of 18.5 dB in SNR. The largest SNR difference is observed around 960 nm wavelength with 21.4 dB increase.

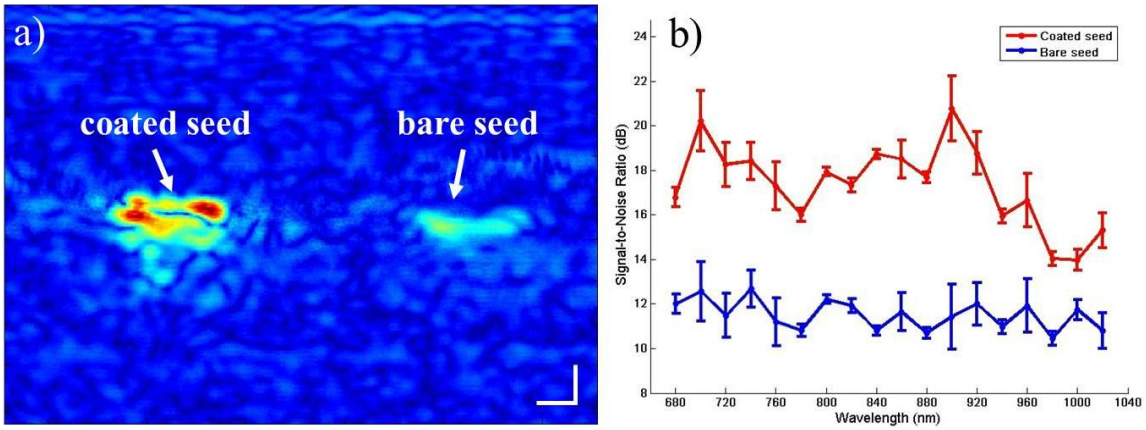

Figure 4.6: (a) PA image of coated and bare seeds under 20mm thick chicken tissue. Horizontal and vertical scale bars denote 2mm. (b) PA spectrum of the coated and bare seeds.

The same spectrum experiment is performed on the phantom with a 2 cm thick chicken tissue in the illumination path. The PA image and the spectrum are shown in Figure 4.6. The mean improvement in SNR is calculated to be 5.9 dB with the largest

increase of 9.3 dB at 900 nm. The spectrum exhibits larger fluctuations in comparison to the one without chicken tissue, likely showing the effect of optical attenuation by the tissue layer. The laser fluence rate during wavelength scanning is maintained as a constant at 15 ± 0.6 mJ/cm^2 for both spectrum experiments.

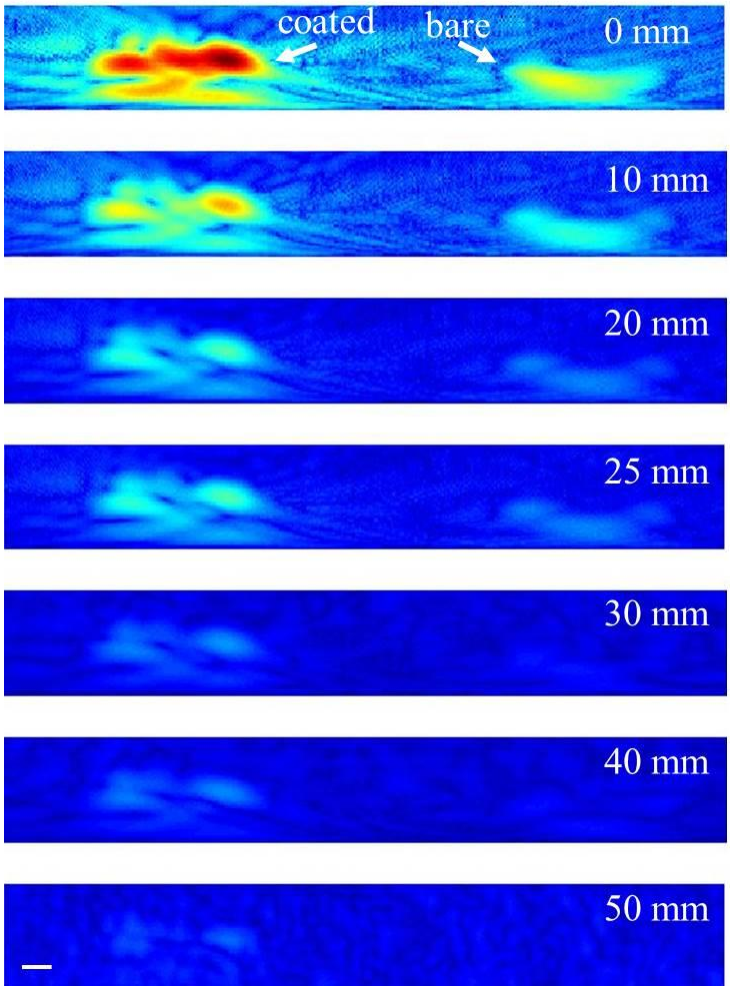

Figure 4.7: PA images of coated and bare seed with increasing imaging depth by layering chicken breast tissue in the illumination path (from 0mm to 50mm). Horizontal scale bar denotes 1 mm.

To demonstrate the improvement in depth imaging, the excitation wavelength is fixed at 700 nm while the imaging depth is increased by adding layers of chicken breast

tissue from 0 mm up to 50 mm thickness. The local fluence rate on the surface is kept at 20 mJ/cm^2. Figure 4.7 shows the resulting images of the coated and bare seed at various depths. The improvement is clear where the bare seed becomes undetectable at depths greater than 25 mm while coated seed is still visible at 50 mm depth. The SNR of each seed is plotted against the imaging depth in Figure 4.8.

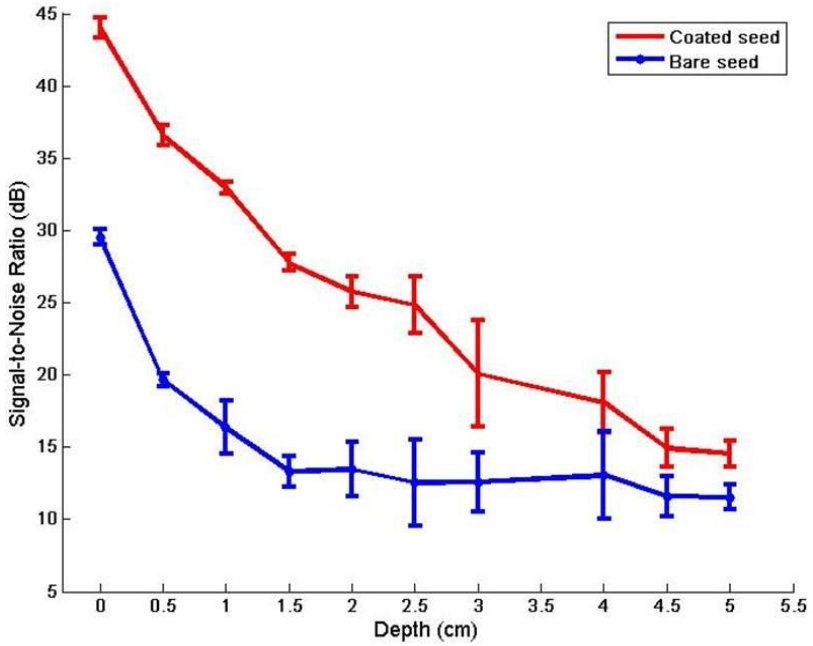

Figure 4.8: SNR of coated seed and bare seed as optical penetration depth increases from 0 to 5 cm

For multiple seeds imaging, three coated and three bare seeds are placed on a previously hardened gelatin phantom and a gelatine solution is poured on top to subsequently cool and adhere to the bottom layer. Once the top layer hardens, the embedded seeds are constrained to be in-plane with the ultrasound transducer. Figure 4.9 (a) and (b) shows the B-mode image and PA image of two columns of seeds in the gelatin phantom. The left column is all coated seeds and the right column is all bare

seeds. Since no needle is used in embedding these seeds, there is no air gap present and US can clearly detect the first two rows of seeds. The last row of seeds, however, is barely detected due to acoustic shadowing from the seeds in the front. The same shadowing effect is also observed in the PA images. The same phantom is covered with 5 cm thick chicken tissue and the result is shown in Figure 4.9 (c). As expected from the previous result, bare seeds are no longer detectable, while the first two coated seeds are still generating enough PA contrast. The last coated seed suffers in contrast due to the combined effect of acoustic shadowing and attenuated illumination energy.

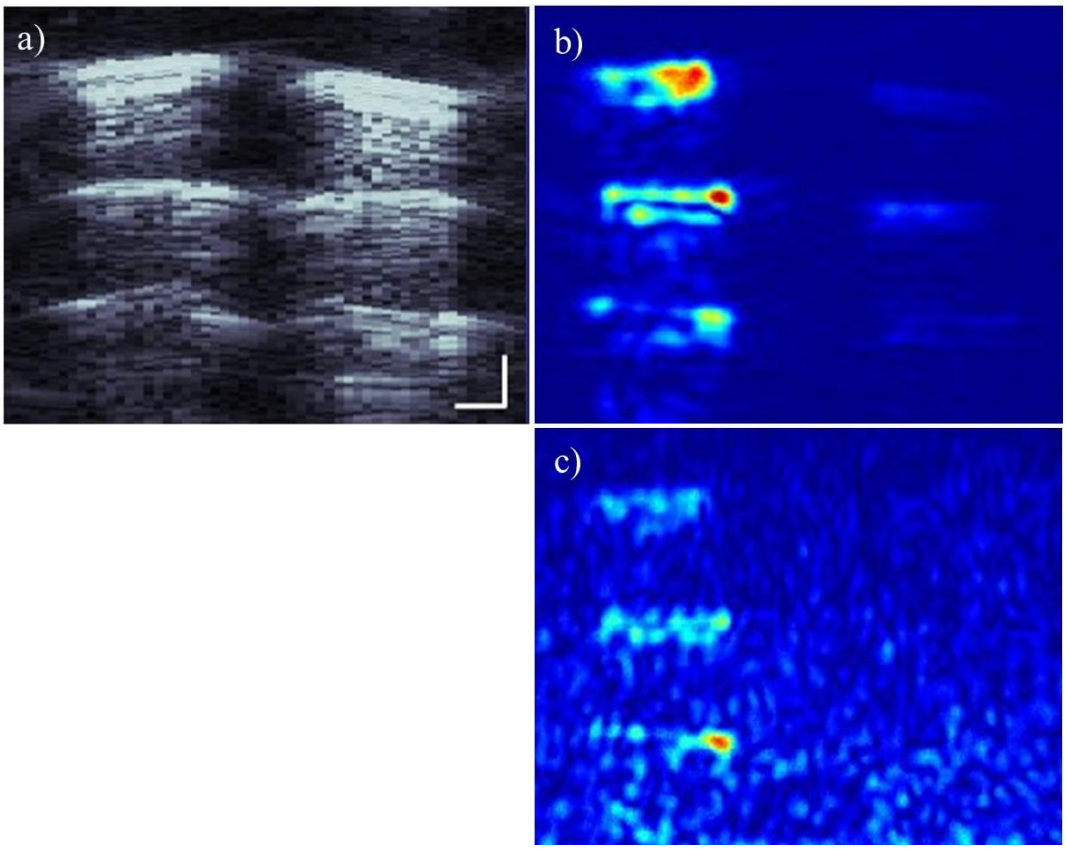

Figure 4.9: (a) B-mode and (b) PA image of three coated seeds (left column) and three bare seeds (right column) in gelatin phantom. (c) PA image of the same phantom with 5 cm of chicken tissue in the path of the illumination light (700 nm). PA images are displayed on the same dynamic range with image intensity in (c) amplified by 20 times for visibility. Scale bars denote 2 mm.

4.2.2 Silver coated seeds

Gold or silver nanoparticles have increasingly become a popular choice for contrast enhancing agent in PA imaging. These metallic nanoparticles have been reported to be highly biocompatible and can absorb NIR light multiples to orders of magnitude higher than biological tissue [31,67–69]. The basic principle behind the increased optical absorption is attributed to a physical phenomenon known as the localized surface plasmon resonance (SPR) effect [70]. When photons impact the nanoparticles, they excite the conduction electrons on the surface. The metal particles then exert a restoring force on the electron cloud [71]. The opposing effects of the photons and the restoring force lead to an oscillation, which has a resonance frequency and localized SPR effect takes place when the incoming photons match the resonance frequency. At such point, the photons are most effectively coupled to the nanoparticles, maximizing the optical absorption efficiency [72].

In this proposed coating method, a layer of silver is deposited onto the brachytherapy seeds. The roughness of the seed surface may lead to uneven deposition of silver particles, which, in turn, may resemble randomly distributed islands of silver of varying sizes.

The actual coating method is based on a previously published coating technique for depositing silver onto titanium dioxide (TiO_2) nanowires by Wen et al [73]. A pair of bare brachytherapy seeds is placed in a container with 20 mL de-ionized water, 10 mL ethanol, 0.5 mL of 1.0 M sodium hydroxide (NaOH), and 0.5 g of silver nitrate ($AgNO_3$). The container is immersed in a temperature controlled water bath maintained at 50 ℃ for

16 hours. The principle deposition mechanism is the reduction of Ag^{+} ions to solid Ag particles by the presence of ethanol in the solution [74]. Figure 4.10 shows the digital photos of bare and coated seeds at 7X magnification. These images are captured by using a stereo microscope (Fisher Scientific, NH, USA) coupled with a CCD camera (DS-5M-U1, Nikon, Japan). They demonstrate the success of the coating process, where in contrast to the metallic and lustrous outer surface of the bare seed, the coated seed shows less reflective surface due to the deposition of Ag particles.

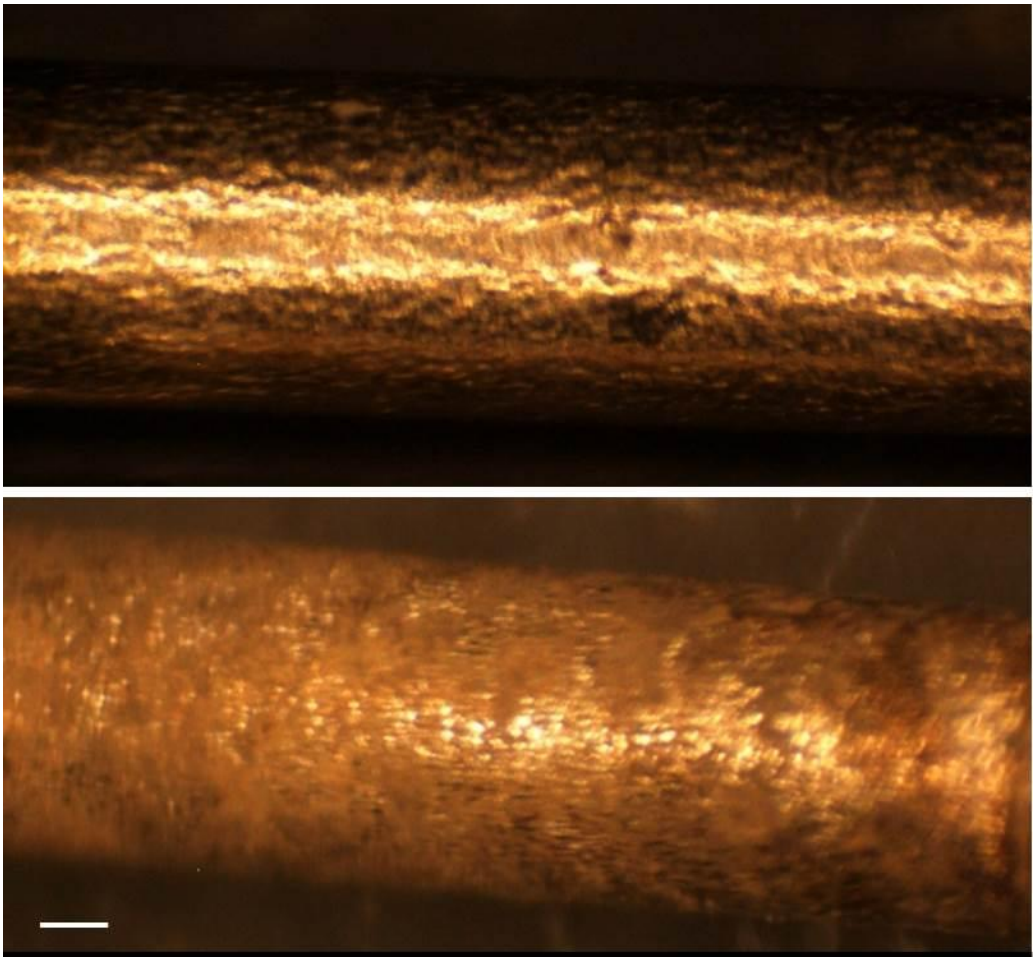

Figure 4.10**:** Digital photos of bare seed (top) and coated seed (bottom) at 7X magnification. Scale bar denotes 0.1 mm.

To demonstrate the PA contrast improvement in the silver coated seed, it is embedded in gelatin phantom next to a bare seed. Excitation wavelength is tuned from 700 nm to 975 nm at 25 nm steps to obtain the PA spectrum of each seed, and the results for two pairs of silver coated and bare seeds are shown in Figure 4.11 and 4.12. On average, the silver coated seed shows a 4.9 dB increase in PA intensity compared to the bare seed for both sets of phantoms. The improvement of silver coating is less pronounced than our first method. The lack of a peak in the spectrum of the coated seed illustrates either that the localized SPR does not take effect within the wavelengths tested or the coating is not successful in creating nano-sized silver islands on the seed. The fact that the deposited silver is observable by naked eyes suggests that silver may have been over deposited onto the seed. More iterations of this coating method with varying time length and reagents concentrations can be run to test for the feasibility of this method in generating localized SPR effect in the future.

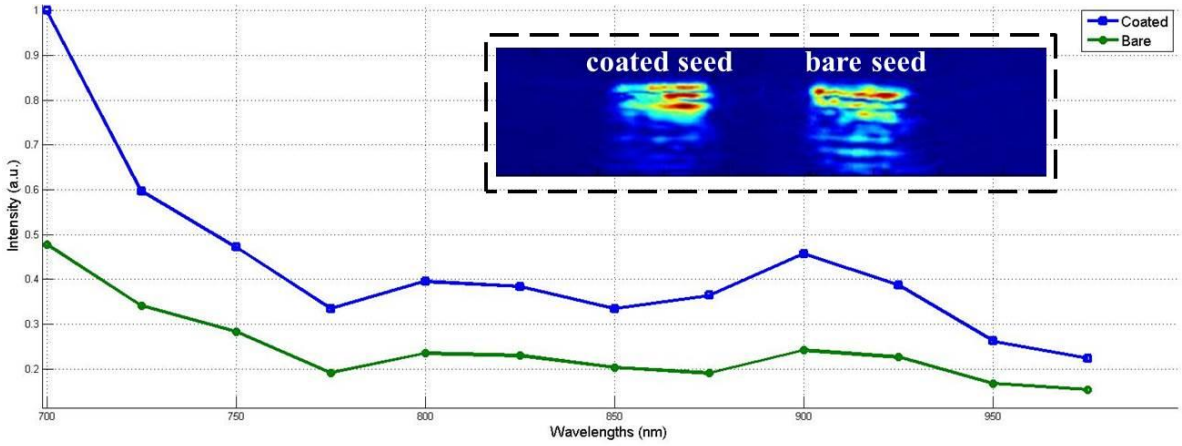

Figure 4.11: PA spectra of the first pair of silver coated and bare seed. Inset shows the PA image of both seeds.

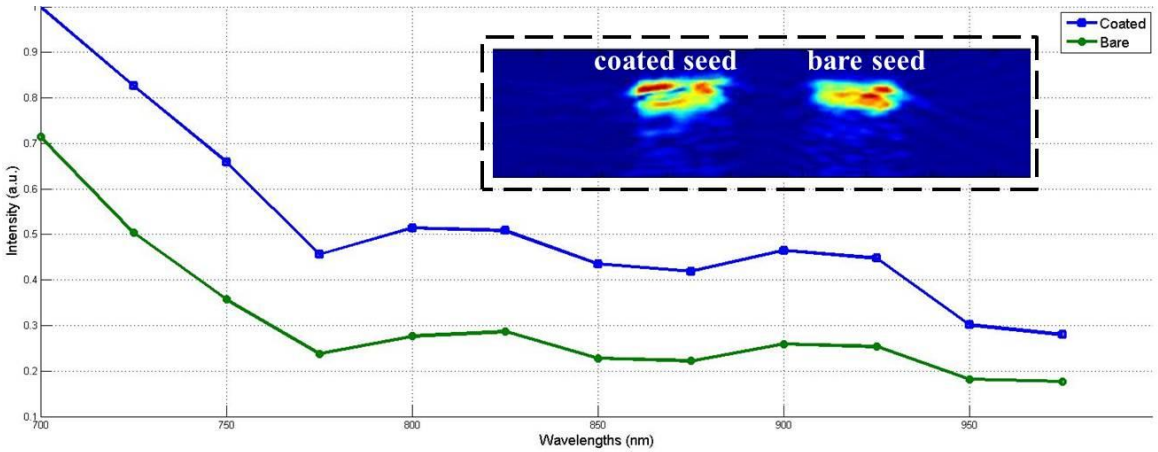

Figure 4.12: PA spectra of the second pair of silver coated and bare seed. Inset shows the PA image of both seeds.

4.3 Ethanol as contrast agent

During a prostate brachytherapy procedure, the brachytherapy seeds are inserted into the patient as either individual seeds or a strand of several seeds held together by certain bio-compatible material. Between each seed in a strand, there is typically a seed length of empty space. In this section, we demonstrate that these spaces can be filled with certain material that acts as a contrast enhancing agent. This method does not require any modifications to the seed itself.

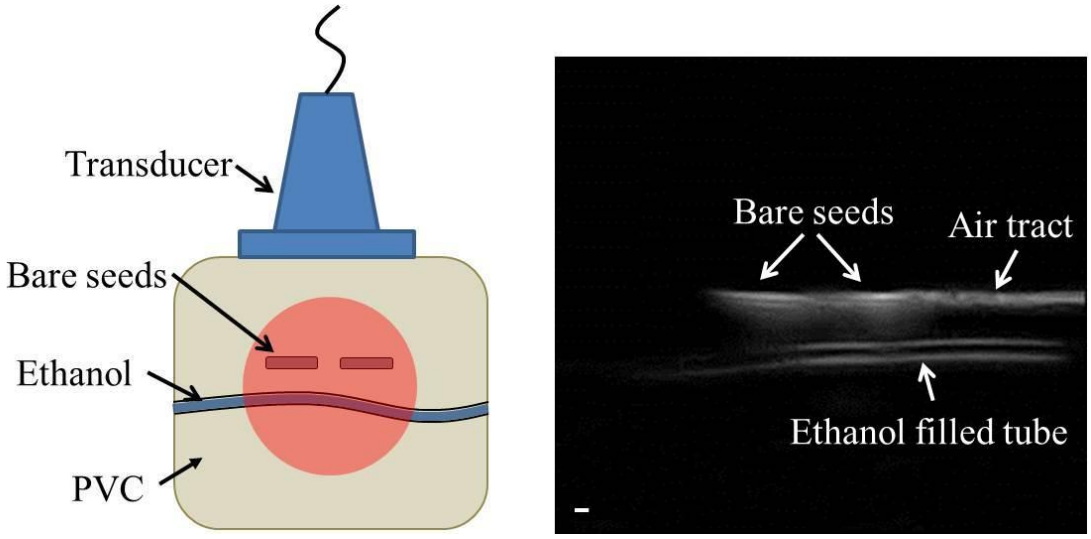

Figure 4.13: Top view of the phantom setup. Two bare seeds and a 0.8 mm inner diameter clear tube filled with ethanol were inserted into the PVC phantom. The red disk represents the illumination area. The drawing is not to scale. The B-mode image of the phantom is shown on the right. Scale bar denotes 1 mm.

Figure 4.13 illustrates the phantom setup. Two bare seeds are inserted via a brachytherapy needle into a PVC phantom. A clear tube in which the ethanol is injected into is inserted behind the seeds. The walls of the tube can be seen from the B-mode image, whereas the seeds are difficult to identify due to the gap of air left behind by the needle. Ethanol is chosen as the contrast enhancing agent. As stated by Equation 2.3, the initial pressure rise from the PA effect is a function of several parameters which includes the isobaric expansion coefficient (β) of the sample. Ethanol (1.5×10^{-3} K^{-1}) has a much larger expansion coefficient than both stainless steel (51.9×10^{-6} K^{-1}) or titanium (25.8×10^{-6} K^{-1}) [75]. Despite the high expansion coefficient, ethanol has negligible absorption at around 700 nm where this experiment was carried out on. Market bought blue food dye solution was therefore added to the absolute ethanol at 20% by volume ratio.

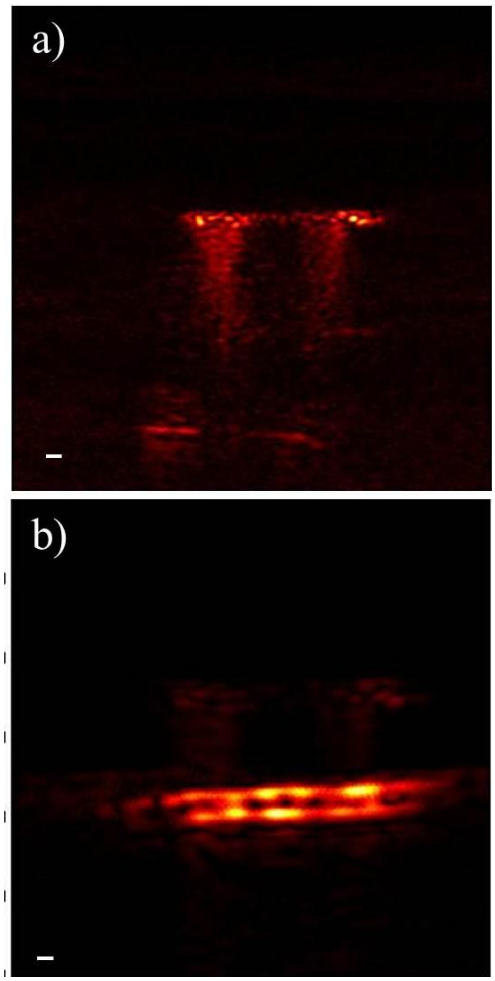

Figure 4.14: (a) PA image of the phantom before the injection of ethanol; and (b), PA image of the phantom after ethanol injection. Image brightness in (a) is increased by 5 fold.

Figure 4.14 shows the PA images of the phantom before and after the injection of dyed ethanol. Before the injection, only the seeds are visible since air within the tube does not generate any PA signal (Figure 4.14 (a)). Once the dyed ethanol is injected, the PA intensity of the dyed ethanol overwhelms the seeds. SNR of the injected dyed ethanol is 10 dB higher than the seeds. Figure 4.15 shows a series of PA images of blue ethanol filled tube in PVC phantom as layers of chicken tissue are added to the path of illumination. There is improvement in the imaging depth, where dyed ethanol can be

seen clearly at 35 mm and vaguely at 45 mm depth in comparison to 25 mm achieved by bare seed as shown in Figure 4.7. This experiment demonstrates that dyed ethanol can be a potential contrast enhancing agent for prostate brachytherapy. Further experiment can be performed by testing different methods of dyeing the ethanol solution or using other high absorption contrast agents, since optical absorption is a key parameter in PA contrast generation.

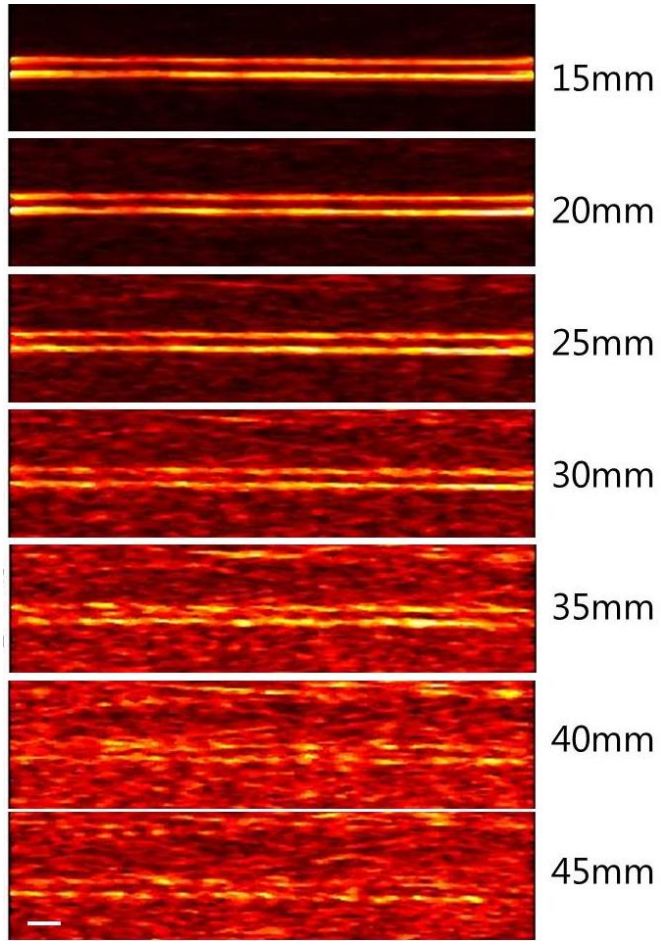

Figure 4.15: PA images of ethanol filled tube with increasing imaging depth. To increase the depth, layers of chicken breast tissue of different thickness were introduced in the illumination path (from 15mm to 45mm). The intensity is normalized within each frame in order to show the weak signal at deeper depth. The relative intensities among the frames are not directly comparable. The scale bar denotes 1 mm.

Chapter 5: Tissue Typing

Despite ongoing advancement in image quality of both PA and US imaging, there are still many limitations. For instance, the detection of small cancerous tissue regions in some organs can be difficult [76,77]. Therefore, an accurate method of characterizing and differentiating tissue pathology in addition to the conventional imaging method is highly beneficial. In PA and US imaging, frequency-domain analysis of the detected signals has shown great promise in quantitative tissue characterization [15,78,79]. Frequency-domain analysis is often exploited due to the fact that acoustic scattering and absorption in tissue are frequency-dependent processes that are affected by the microstructure of the tissue. In PA imaging, however, tissue information is not limited merely in the frequency-domain.

In this chapter, a novel intensity-based method of tissue typing between fatty and non-fatty tissue is presented. As mentioned in Chapter 1.3, this method is based on the fact that PA intensity is a function of speed of sound of the illuminated tissue and the speed of sound itself has tissue specific dependence on temperature. By introducing a temperature change to the tissue samples and acquiring PA images through the process, we aim to differentiate between the two types of tissues through analyzing the PA intensity change. The specific heating and analysis method are presented with results from several samples tabulated.

5.1 Methods

As shown in Chapter 2.2, the initial pressure rise caused by the PA effect has a dependence on several parameters of the tissue sample, two of which are the isobaric volume expansion coefficient, and speed of sound. Both of these parameters are temperature dependent. As Figure 5.1 illustrates, the rate of change of speed of sound in non-fatty tissue such as liver is 1.83 m/(℃·s) and in fat is -10.1 m/(℃·s) for fat at room temperature. This opposite dependence on temperature is expected to be directly reflected in the change of the PA intensity, and we aim to differentiate between the two types of tissue by analyzing the intensity change.

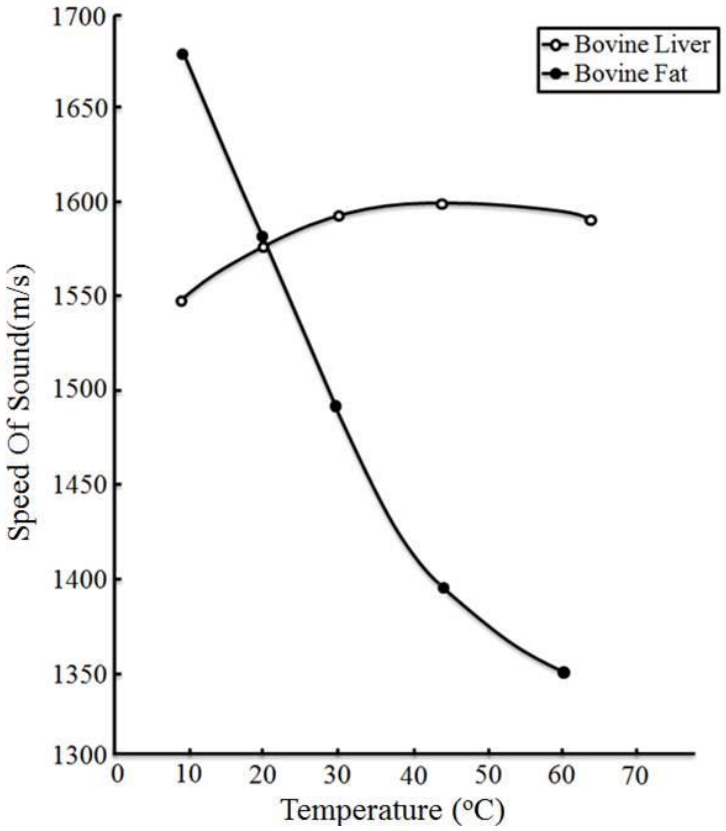

Figure 5.1: Speed of sound of water-based bovine liver and fatty-based bovine fat as a function of temperature. Figure adapted from [33].

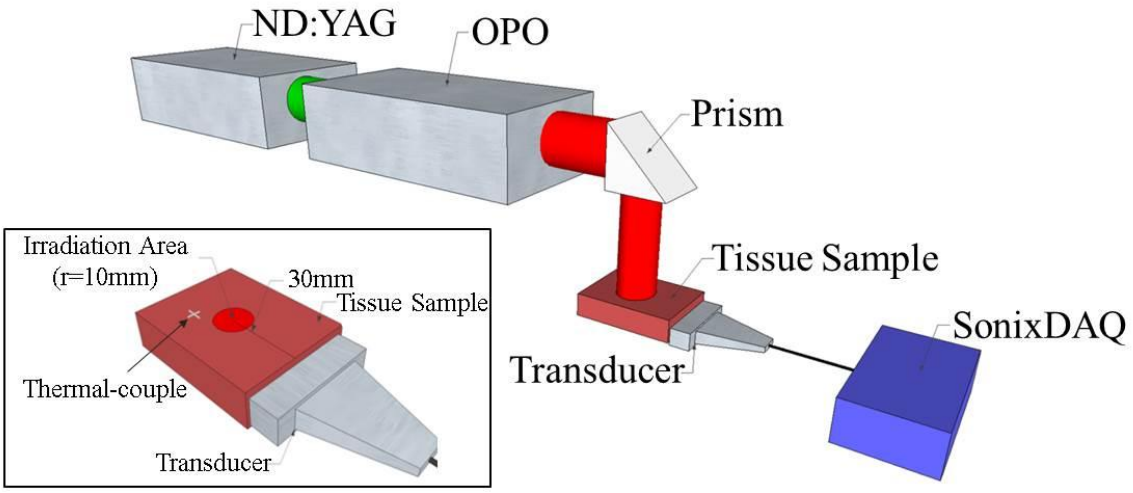

Figure 5.2: Setup diagram of the PA system for tissue typing experiment. Inset shows the location of thermal-couple insertion for monitoring relative temperature change in the tissue sample.

A PA imaging setup similar to the previous chapter is used as shown in Figure 5.2. Two tissue types are analyzed *ex-vivo* in this study: bovine fat and porcine liver. For the first experiment, samples are cooled to approximately 10 ℃ by a refrigerator prior to the start of the experiment. Once the sample is removed from cooling and put in place for data acquisition, a thermocouple is inserted near the irradiation region to continuously monitor the temperature rise as the sample gradually returns to room-temperature at around 17 ℃. For every 0.5 ℃ rise in the temperature, ten frames of PA image are recorded and averaged. In total, fifteen sets of PA image data over a 7 ℃ rise in temperature are acquired and analyzed. Wavelengths of 700 nm and 920 nm are selected for porcine liver and bovine fat samples respectively. The specific wavelength is chosen for bovine fat because fatty tissue has an absorption peak around such wavelength [80]. For a blood-rich tissue such as the liver, haemoglobin is the main tissue constituent and a shorter wavelength is used to maximize the optical absorption.

5.2 Room temperature heating result

Figures 5.3 and 5.4 show a series of PA images of the porcine liver and bovine fat samples at six temperature intervals. Every image is an average of ten frames, and is normalized to the brightest image in each series of the images (Figure 5.3 (f), and Figure 5.4 (a) respectively). For the liver sample, the PA intensity increases towards higher temperature. The opposite change in PA signal intensity is observed in bovine fat samples.

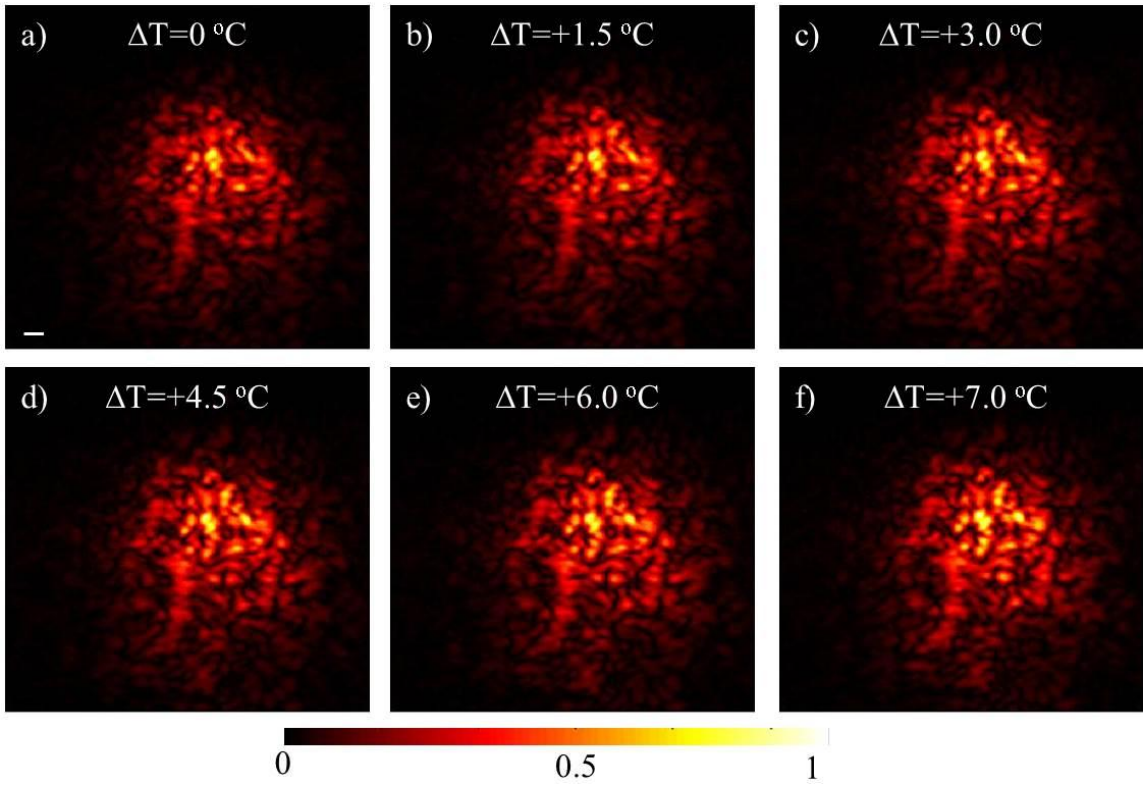

Figure 5.3: PA images of porcine liver at six temperature intervals. Scale bar denotes 1 mm.

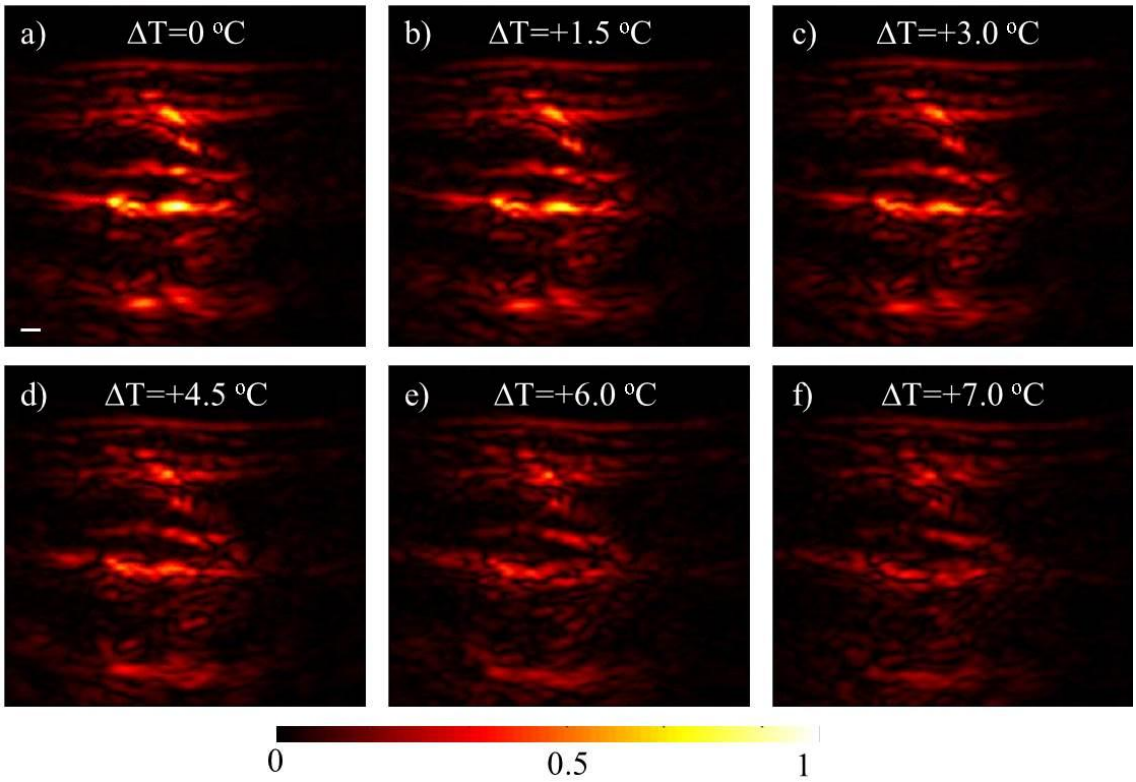

Figure 5.4: PA images of bovine fat at six temperature intervals. Scale bar denotes 1 mm.

The intensity change of the series of images over the entire temperature range is plotted in Fig. 5.5. The liver sample shows an increase of 2.82 %/℃, and the fat sample shows a decrease of 6.24 %/℃. A larger change in the signal intensity in the fat sample is expected since fatty tissue also has a larger magnitude of change in its speed of sound value as temperature increases. Speed of sound in fatty tissue, however, decreases nearly six times greater than the increase in the liver tissue. This is not reflected in our results whereas the magnitude of slope of the bovine fat sample is roughly two times greater than the liver sample. In addition to the sample-to-sample variations in the dependence factor, such discrepancy can also be attributed to the temperature dependence of the acoustic attenuation of both samples. The acoustic attenuation coefficient in both the

liver and fatty tissue decreases as temperature increases from ~10 ℃ toward room-temperature [33]. Since the position of the laser irradiation on the sample is approximately three centimetres away from the surface of the transducer, the generated PA pressure waves are attenuated less while propagating toward the transducer as the temperature rises. This results in the increase of received PA intensity, regardless of the change in the speed of sound. For the liver sample, this increase causes the slope of the intensity curve to be greater. Conversely, a lower rate of intensity decrease is observed from the bovine fat sample.

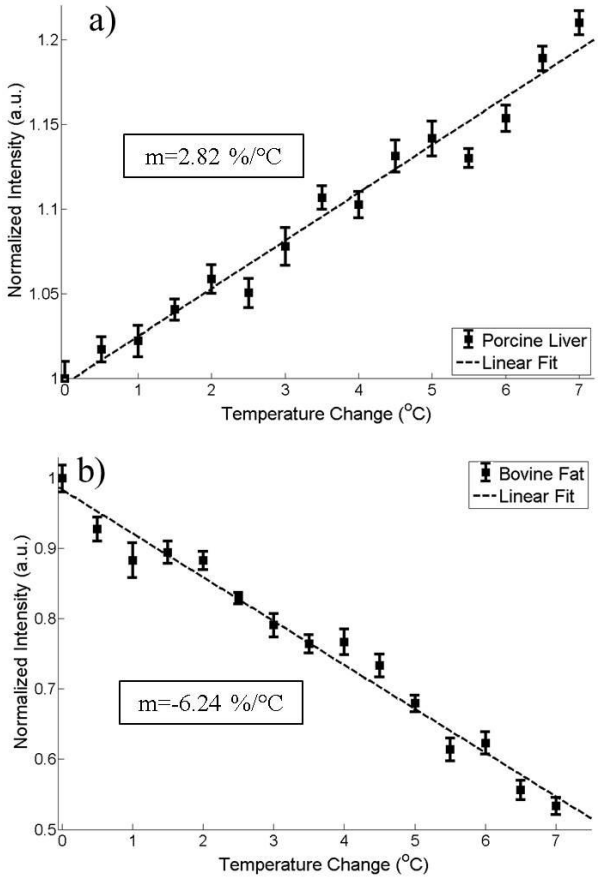

Figure 5.5 Normalized PA signal intensity change over 7 °C temperature increase for (a) porcine liver, and (b) bovine fat. Error bar denotes the standard deviations of ten frames at each measurement. The slope values (m) are +2.82 %/℃ for the liver sample and -6.24 %/℃ for the fat sample.

Table 5.1: Summary of the slope of PA intensity change over 7 ^{o}C temperature increase for five porcine liver and three bovine fat samples tested.

Samples	Porcine Liver (%/℃)	Bovine Fat (%/℃)
#1	2.82	-6.24
#2	2.77	-5.84
#3	2.59	-5.44
#4	3.02	-
#5	2.05	-
Average	**2.6 ±0.4**	**-5.4 ±0.4**

In addition to the samples shown in Figure 5.5, four liver samples and two more fat samples are analyzed and the results are tabulated in Table 5.1. It can be seen that the rates of change in PA intensity as temperature increases are relatively consistent on a sample-to-sample basis.

5.3 Laser heating method

In addition to the previous method where the temperature change is introduced to the sample via room-temperature heating by cooling the samples beforehand, an alternative method of heating is tested. In this method, tissue samples are kept at room-temperature. To heat up the sample, the laser is turned to repeatedly firing at 10 Hz rate for an entire minute, and at each pulse of laser a frame of PA image is acquired. In total, 600 PA frames are captured as a set for each sample. There are two advantages in this method of heating. Firstly, for future *in-vivo* experiment, it is not practical or safe to the subject to introduce a temperature change as large as 7 ^{o}C. Heating through the laser seems to be a viable option without the need for any extra equipment for a separate heating mechanism. Secondly, laser heating only introduces a temperature increase

localized to the region of illumination. This should alleviate the effect of the temperature dependence of acoustic attenuation in the surrounding tissue, which can affect the PA intensity change as discussed in the previous section.

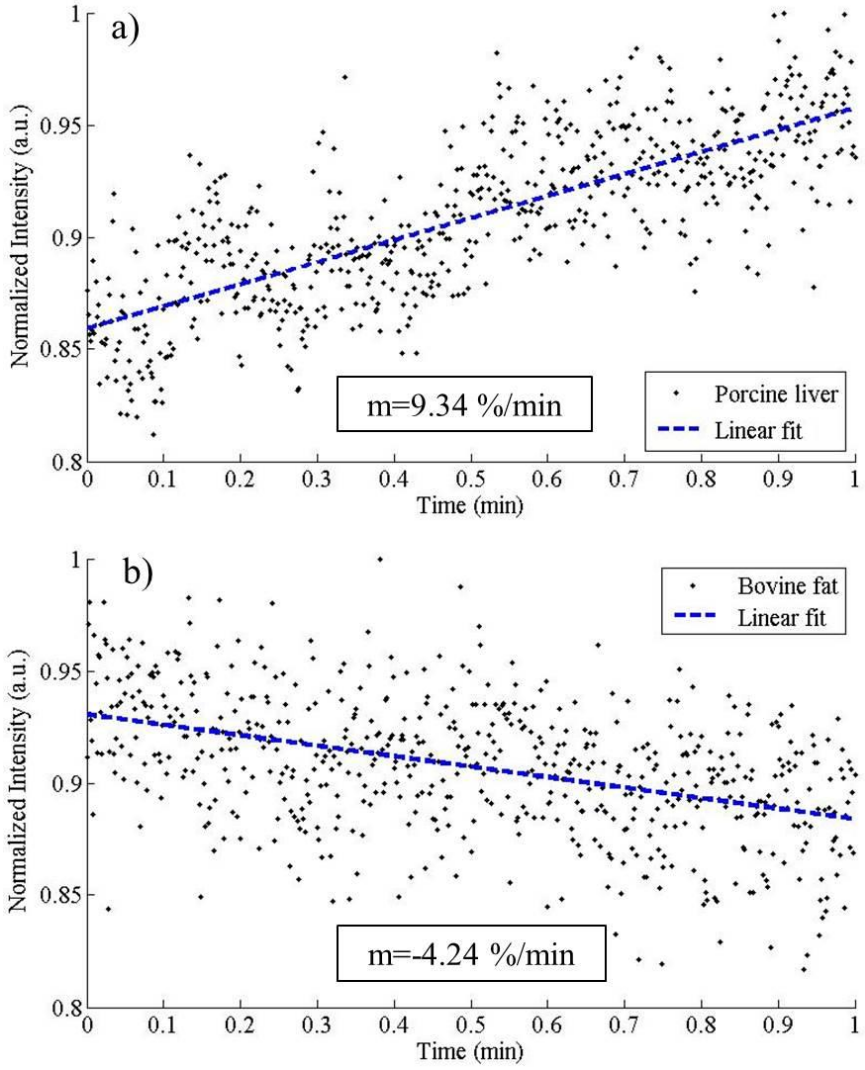

Figure 5.6: PA intensity of (a) porcine liver and (b) bovine fat over a minute of continuous heating and frame acquisition. Linear fit through the data points shows an increase of 9.34 %/min and a decrease of 4.4 %/min for the porcine liver and the bovine fat respectively.

Figure 5.6 shows the normalized PA intensity of the top 10 % pixel values of each sample. The PA intensity increases in the porcine liver sample (9.34 %/min), and

decreases in the bovine fat sample (-4.24 %/min). The opposite change in PA intensity in the two tissue samples is consistent with room-temperature heating results. Unlike the results from the room-temperature heating method, however, the liver sample has a larger magnitude of change than the fat sample. This is likely because the two tissue samples could experience different amounts of temperature rise through laser heating. In the previous method, the temperature of the samples is monitored by a thermal-couple, and the room air acting as the heating source means that both tissue samples are heated toward the same temperature, albeit at slightly different rate. With laser heating, however, the amount of heating has large dependence on how efficiently each region of tissue converts the illuminatin photon energy into heat, which is largely a function of optical absorption. It is likely that the higher optical absorption coefficient of haemoglobin, which is the major chromophore in liver, allows porcine liver tissue to be heated much quicker than bovine fat tissue.

Table 5.2 summarizes the rate of change in PA intensity for five liver and five fat samples. A relatively large variation is observed in both samples. If we assume that the laser fluence rate is more or less constant for all samples measured, then the sample to sample differences suggest a large variation in the optical absorption. Optical absorption, as aforementioned, determines the amount of heat absorbed by the illuminated region. For a single frame of PA image, optical absorption can be quantified by analyzing the image intensity. For samples with higher optical absorption, higher image intensity is expected. Figure 5.7 illustrates the relationship between image intensity and the rate of intensity change. The y-value of each data point represents the average intensity of the

first 10 frames of each sample summarized in Table 5.2. These points are plotted against the corresponding magnitude of slope value. It can be seen that the liver samples generally have higher intensity than the fat samples. This is explained before as haemoglobin having higher absorption than fat. It can also be seen that higher image intensity usually results in a larger rate of change in the intensity over the duration of heating for both types of samples. Optical absorption alone does not wholly account for the intensity variation amongst the samples. Experimental conditions, such as how close the imaging plane is to the tissue surface, also affect the final image intensity since the laser fluence rate depends on the imaging depth. Sample to sample variation also contributes to the observed variation in our results. Nonetheless, the liver samples show a positive slope and the fat samples shows a negative slope in the rate of change in the PA intensity over one minute of laser heating. Therefore, the proposed method is useful in differentiating between fatty and non-fatty tissues.

Table 5.2: Summary of the slope of PA intensity change over 1 min of laser heating for six porcine liver and five bovine fat samples measured.

Samples	Porcine Liver (%/min)	Bovine Fat (%/min)
#1	9.34	-4.24
#2	7.25	-2.69
#3	6.50	-3.86
#4	5.39	-3.25
#5	6.13	-6.76
Average	**6.9 ±1.5**	**-4.2 ±1.5**

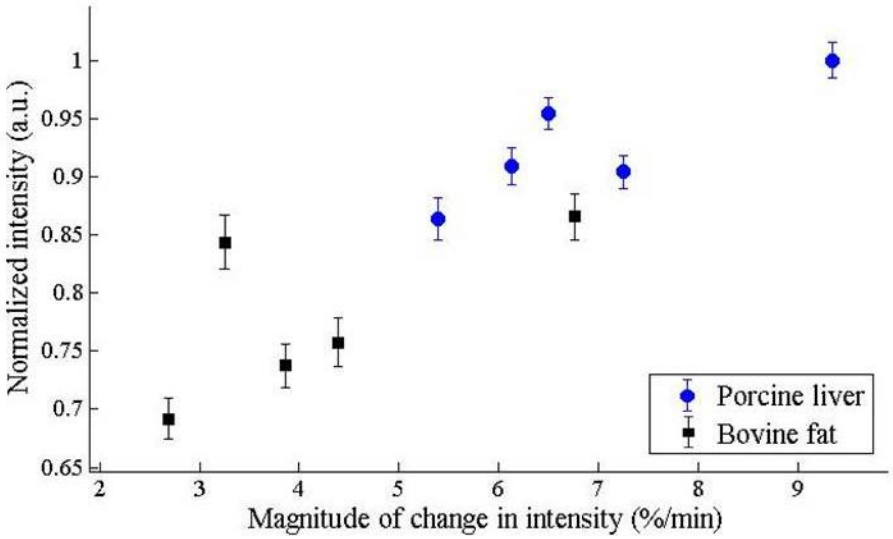

Figure 5.7: Normalized average intensity of the first ten frames of each sample data plotted against the magnitude of change in its intensity.

Chapter 6: Conclusion

Photoacoustic imaging is a hybrid modality that relies on photons for signal generation, and sound for signal propagation. Such bi-modal nature of the system allows for deeper imaging depth than conventional optical modality while maintaining spatial resolution in the US imaging range. It is also able to perform functional imaging such as blood oxygenation measurement due to its optical absorption based contrast mechanism. Due to these advantages, and its ease of integration with current US systems for multimodal imaging, PA imaging has been researched extensively in recent years. Optical attenuation limited imaging depth is still a major obstacle of successful imaging of brachytherapy seeds embedded farther away from the transducer. The first part of this thesis aims to improve the PA contrast of the seeds for deeper imaging depth by modifying the seeds directly. The second part of this thesis proposes a novel method in tissue typing using PA imaging.

This chapter explains the significance of the work done, and suggests possible future directions.

6.1 Significance of work

Many groups have proposed various modified reconstruction algorithms for limited-view PAT imaging system in order to improve the quality and accuracy of reconstruction for deeper imaging depth and higher imaging resolution. We presented an alternative way to improve the PA imaging depth for brachytherapy seeds by modifying the seeds directly. As an initial feasibility test, several methods of seed modifications

were performed and tested. The first method of modification involved using black paint as a layer of absorption enhancing coating. The results showed a significant increase in the PA contrast and detectable depth. Compared to the bare seed, coated seed had on average 18.5 dB increase in its SNR when no optical attenuating layer of tissue was in the light path. When layers of tissue were placed to simulate deeper imaging depth, coated seed was detected as deep as 5 cm whereas bare seed became difficult to distinguish at 2.5 cm. The second method of coating through chemical reduction of silver ions also showed a noticeable improvement in PA contrast. An average of 5 dB in PA intensity was observed for the silver coated seeds. These methods demonstrated the potential of imaging improvement through seeds modification. Using dyed ethanol solution as the space filling solution between seeds also showed improvement in the PA intensity comparable to that of the black paint method.

The intensity-based tissue typing method proposed also successfully differentiated between fatty and non-fatty tissue such as the porcine liver and bovine fat samples measured *ex-vivo*. Room-temperature heating method showed an average increase in PA intensity of 2.6 ± 0.4 %/℃ in five samples of porcine liver, and an average decrease of 5.4 ± 0.4 %/℃ in three samples of bovine fat. With the laser as heating source, the average increase of PA intensity in porcine liver was 6.9 ± 1.5 %/min, and the average decrease in bovine fat was 4.2 ± 1.5 %/min. It is clear that with either method, the PA intensity change as a function of temperature differs significantly between the two tissue types. Our results show that PA imaging can potentially have important applications in brachytherapy and tissue typing.

In addition to the contrast enhancing and tissue typing methods, the success of building a working PA imaging system is significant and essential for future projects to be carried out by the others.

6.2 Future work and improvement

For the PA imaging system design, we are still at the bench-top stage. The next step is the integration between the light source and the transducer. This can be achieved through coupling the excitation light into optical fibre bundles which can be physically mounted to the transducer. A hand-held probe will allow the possibility of *in-vivo* experiments. The main challenge is how to maximize the coupling efficiency of the light into the fibres, since the fluence rate of the laser affects the image quality greatly.

The studied coating methods of the brachytherapy seeds are merely a proof-of-concept to demonstrate the possibility in such approach. Physical deposition methods such as sputtering or molecular beam epitaxy can provide a better controlled coating of PA contrast enhancing material such as silver on the seeds. Alternatively, a method of binding gold nanoparticles onto the seeds can be looked into as the nanoparticles can have high optical absorption and bio-compatibility. Spaces between seeds have been shown to provide a possible source of contrast enhancement through the dyed ethanol experiment. It can be further expanded to test for other bio-compatible solutions with high optical absorption or expansion coefficient. One suitable candidate is the use of aforementioned gold nanoparticles in solution as the space filler. Since the optical absorption peak of the gold nanoparticles can be tuned by altering the particle size, the nanoparticles used for coating the seeds can have a different absorption peak from the

ones used in the filler. This can allow targeted imaging of either the seeds or the spaces through tuning the laser wavelength.

For tissue typing, a variety of tissue types can be tested to verify the extent to which the proposed tissue typing method can be performed on. It is of great interest to see whether the proposed method can differentiate two types of tissues from the same group such as liver and muscle which are both considered to be non-fatty tissue. Improvement on the method of analysis can also be made. Currently, the change in PA intensity is calculated from averaging the top 10% pixel value of each PA image. For one set of tissue sample, only a single value of rate of change of intensity is obtained through this method. For a set of data with the laser-heating method, where a large number of frames of data is available, an alternative analysis method is to divide each frame into smaller ROIs and calculate the corresponding rate of change in PA intensity for each ROI. For imaging samples with both fatty and non-fatty tissue types, such a method can visually display and differentiate regions of fatty and non-fatty tissue. Another suggestion would be combining the US based tissue typing method with the PA based one by acquiring time series data of US data interlaced with PA data. Since the two modalities have different contrast generating mechanisms, the combination of the two methods may lead to an improved tissue typing accuracy.

Bibliography

[1] J.-T. Oh, M.-L. Li, H. F. Zhang, K. Maslov, G. Stoica, and L. V. Wang, "Three-dimensional imaging of skin melanoma in vivo by dual-wavelength photoacoustic microscopy," *J. Biomed. Opt.* **11**(3), 34032 (2006) [doi:10.1117/1.2210907].

[2] J. Laufer, P. Johnson, E. Zhang, B. Treeby, B. Cox, B. Pedley, and P. Beard, "In vivo preclinical photoacoustic imaging of tumor vasculature development and therapy," *J. Biomed. Opt.* **17**(5), 0560161–0560168 (2012) [doi:10.1117/1.JBO.17.5.056016].

[3] R. O. Esenaliev, A. A. Karabutov, F. K. Tittel, B. D. Fornage, S. L. Thomsen, C. Stelling, and A. A. Oraevsky, "Laser optoacoustic imaging for breast cancer diagnostics: limit of detection and comparison with x-ray and ultrasound imaging," 1997, 71–82 [doi:10.1117/12.280213].

[4] X. Wang, Y. Pang, G. Ku, G. Stoica, and L. V. Wang, "Three-dimensional laser-induced photoacoustic tomography of mouse brain with the skin and skull intact," *Opt. Lett.* **28**(19), 1739–1741 (2003) [doi:10.1364/OL.28.001739].

[5] N. Kuo, H. J. Kang, D. Y. Song, J. U. Kang, and E. M. Boctor, "Real-time photoacoustic imaging of prostate brachytherapy seeds using a clinical ultrasound system," *J. Biomed. Opt.* **17**(6), 066005 (2012) [doi:10.1117/1.JBO.17.6.066005].

[6] J. Tyndall, "Action of an Intermittent Beam of Radiant Heat upon Gaseous Matter," *Proc. R. Soc. Lond.* **31**(206-211), 307–317 (1880) [doi:10.1098/rspl.1880.0037].

[7] A. G. Bell, "Upon the production and reproduction of sound by light," *J. Soc. Telegr. Eng.* **9**(34), 404–426 (1880) [doi:10.1049/jste-1.1880.0046].

[8] C. K. N. Patel and A. C. Tam, "Pulsed optoacoustic spectroscopy of condensed matter," *Rev. Mod. Phys.* **53**(3), 517–550 (1981) [doi:10.1103/RevModPhys.53.517].

[9] A. C. Tam, "Applications of photoacoustic sensing techniques," *Rev. Mod. Phys.* **58**(2), 381–431 (1986) [doi:10.1103/RevModPhys.58.381].

[10] T. Bowen, "Radiation-Induced Thermoacoustic Soft Tissue Imaging," in *1981 Ultrason. Symp.*, pp. 817–822 (1981) [doi:10.1109/ULTSYM.1981.197737].

[11] R. A. Kruger, P. Liu, Y. "'Richard'" Fang, and C. R. Appledorn, "Photoacoustic ultrasound (PAUS)—Reconstruction tomography," *Med. Phys.* **22**(10), 1605–1609 (1995) [doi:10.1118/1.597429].

[12] G. Ku and L. V. Wang, "Scanning thermoacoustic tomography in biological tissue," *Med. Phys.* **27**(5), 1195–1202 (2000) [doi:10.1118/1.598984].

[13] C. G. A. Hoelen, F. F. M. de Mul, R. Pongers, and A. Dekker, "Three-dimensional photoacoustic imaging of blood vessels in tissue," *Opt. Lett.* **23**(8), 648–650 (1998) [doi:10.1364/OL.23.000648].

[14] M. Xu and L. V. Wang, "Universal back-projection algorithm for photoacoustic computed tomography," *Phys. Rev. E Stat. Nonlin. Soft Matter Phys.* **71**(1 Pt 2), 016706 (2005).

[15] R. E. Kumon, C. X. Deng, and X. Wang, "Frequency-Domain Analysis of Photoacoustic Imaging Data From Prostate Adenocarcinoma Tumors in a Murine Model," *Ultrasound Med. Biol.* **37**(5), 834–839 (2011) [doi:10.1016/j.ultrasmedbio.2011.01.012].

[16] Y. Lao, D. Xing, S. Yang, and L. Xiang, "Noninvasive photoacoustic imaging of the developing vasculature during early tumor growth," *Phys. Med. Biol.* **53**(15), 4203–4212 (2008) [doi:10.1088/0031-9155/53/15/013].

[17] Meng-Lin Li, Jung-Taek Oh, Xueyi Xie, Geng Ku, Wei Wang, Chun Li, G. Lungu, G. Stoica, and L. V. Wang, "Simultaneous Molecular and Hypoxia Imaging of Brain Tumors In Vivo Using Spectroscopic Photoacoustic Tomography," *Proc. IEEE* **96**(3), 481–489 (2008) [doi:10.1109/JPROC.2007.913515].

[18] B. Yin, D. Xing, Y. Wang, Y. Zeng, Y. Tan, and Q. Chen, "Fast photoacoustic imaging system based on 320-element linear transducer array," *Phys. Med. Biol.* **49**(7), 1339–1346 (2004).

[19] S. A. Ermilov, T. Khamapirad, A. Conjusteau, M. H. Leonard, R. Lacewell, K. Mehta, T. Miller, and A. A. Oraevsky, "Laser optoacoustic imaging system for detection of breast cancer," *J. Biomed. Opt.* **14**(2), 024007–024007–14 (2009) [doi:10.1117/1.3086616].

[20] R. A. Kruger, R. B. Lam, D. R. Reinecke, S. P. Del Rio, and R. P. Doyle, "Photoacoustic angiography of the breast," *Med. Phys.* **37**(11), 6096–6100 (2010).

[21] P. Beard, "Biomedical photoacoustic imaging," *Interface Focus* **1**(4), 602–631 (2011) [doi:10.1098/rsfs.2011.0028].

[22] R. E. Peschel and J. W. Colberg, "Surgery, brachytherapy, and external-beam radiotherapy for early prostate cancer," *Lancet Oncol.* **4**(4), 233–241 (2003) [doi:10.1016/S1470-2045(03)01035-0].

[23] X. Wen, S. T. E. Salcudean, and P. D. Lawrence, "Detection of brachytherapy seeds using 3-D transrectal ultrasound," *IEEE Trans. Biomed. Eng.* **57**(10), 2467–2477 (2010) [doi:10.1109/TBME.2010.2053926].

[24] T. Harrison and R. J. Zemp, "Coregistered photoacoustic-ultrasound imaging applied to brachytherapy," *J. Biomed. Opt.* **16**(8), 080502–080502–3 (2011) [doi:10.1117/1.3606566].

[25] J. L. Su, R. R. Bouchard, A. B. Karpiouk, J. D. Hazle, and S. Y. Emelianov, "Photoacoustic imaging of prostate brachytherapy seeds," *Biomed. Opt. Express* **2**(8), 2243–2254 (2011) [doi:10.1364/BOE.2.002243].

[26] M. A. Lediju Bell, N. Kuo, D. Y. Song, and E. M. Boctor, "Short-lag spatial coherence beamforming of photoacoustic images for enhanced visualization of prostate brachytherapy seeds," *Biomed. Opt. Express* **4**(10), 1964–1977 (2013) [doi:10.1364/BOE.4.001964].

[27] C. Huang, A. A. Oraevsky, and M. A. Anastasio, "Investigation of limited-view image reconstruction in optoacoustic tomography employing a priori structural information," 19 August 2010, 780004–780004–6 [doi:10.1117/12.861005].

[28] K. P. Köstli and P. C. Beard, "Two-dimensional photoacoustic imaging by use of Fourier-transform image reconstruction and a detector with an anisotropic response," *Appl. Opt.* **42**(10), 1899–1908 (2003).

[29] G. Paltauf, R. Nuster, M. Haltmeier, and P. Burgholzer, "Experimental evaluation of reconstruction algorithms for limited view photoacoustic tomography with line detectors," *Inverse Probl.* **23**(6), S81–S94 (2007) [doi:10.1088/0266-5611/23/6/S07].

[30] A. Buehler, A. Rosenthal, T. Jetzfellner, A. Dima, D. Razansky, and V. Ntziachristos, "Model-based optoacoustic inversions with incomplete projection data," *Med. Phys.* **38**(3), 1694–1704 (2011) [doi:10.1118/1.3556916].
[31] G. P. Luke, A. Bashyam, K. A. Homan, S. Makhija, Y.-S. Chen, and S. Y. Emelianov, "Silica-coated gold nanoplates as stable photoacoustic contrast agents for sentinel lymph node imaging," *Nanotechnology* **24**(45), 455101 (2013) [doi:10.1088/0957-4484/24/45/455101].
[32] M. Moradi, P. Abolmaesumi, and P. Mousavi, "Tissue typing using ultrasound RF time series: experiments with animal tissue samples," *Med. Phys.* **37**(8), 4401–4413 (2010).
[33] Bamber, J.C. and Hill, C.R., "Ultrasonic attenuation and propagation speed in mammalian tissues as a function of temperature," *Ultrasound Med. Biol.* **5**(2), 149–157 (1979).
[34] R. Seip and E. S. Ebbini, "Noninvasive estimation of tissue temperature response to heating fields using diagnostic ultrasound," *IEEE Trans. Biomed. Eng.* **42**(8), 828–839 (1995) [doi:10.1109/10.398644].
[35] C. Simon, P. VanBaren, and E. S. Ebbini, "Two-dimensional temperature estimation using diagnostic ultrasound," *IEEE Trans. Ultrason. Ferroelectr. Freq. Control* **45**(4), 1088–1099 (1998) [doi:10.1109/58.710592].
[36] T. Varghese, J. A. Zagzebski, Q. Chen, U. Techavipoo, G. Frank, C. Johnson, A. Wright, and F. T. Lee Jr, "Ultrasound monitoring of temperature change during radiofrequency ablation: preliminary in-vivo results," *Ultrasound Med. Biol.* **28**(3), 321–329 (2002) [doi:10.1016/S0301-5629(01)00519-1].
[37] V. E. Gusev, *Laser optoacoustics*, American Institute of Physics, New York (1993).
[38] F. A. Duck, *Physical properties of tissue: a comprehensive reference book*, Academic Press, London (1990).
[39] D.-K. Yao, C. Zhang, K. Maslov, and L. V. Wang, "Photoacoustic measurement of the Grüneisen parameter of tissue," *J. Biomed. Opt.* **19**(1), 017007–017007 (2014) [doi:10.1117/1.JBO.19.1.017007].
[40] G. J. Diebold, T. Sun, and M. I. Khan, "Photoacoustic monopole radiation in one, two, and three dimensions," *Phys. Rev. Lett.* **67**(24), 3384–3387 (1991) [doi:10.1103/PhysRevLett.67.3384].
[41] M. I. Khan and G. J. Diebold, "The photoacoustic effect generated by an isotropic solid sphere," *Ultrasonics* **33**(4), 265–269 (1995) [doi:10.1016/0041-624X(95)00034-Z].
[42] V. G. Andreev, A. A. Karabutov, and A. A. Oraevsky, "Detection of ultrawide-band ultrasound pulses in optoacoustic tomography," *IEEE Trans. Ultrason. Ferroelectr. Freq. Control* **50**(10), 1383–1390 (2003) [doi:10.1109/TUFFC.2003.1244756].
[43] V. Ntziachristos, "Going deeper than microscopy: the optical imaging frontier in biology," *Nat. Methods* **7**(8), 603–614 (2010) [doi:10.1038/nmeth.1483].
[44] R. H. Webb, "Confocal optical microscopy," *Rep. Prog. Phys.* **59**(3), 427 (1996) [doi:10.1088/0034-4885/59/3/003].
[45] V. Andresen, S. Alexander, W.-M. Heupel, M. Hirschberg, R. M. Hoffman, and P. Friedl, "Infrared multiphoton microscopy: subcellular-resolved deep tissue imaging," *Curr. Opin. Biotechnol.* **20**(1), 54–62 (2009) [doi:10.1016/j.copbio.2009.02.008].

[46] L. V. Wang and H.-I. Wu, “Ballistic Imaging and Microscopy,” in *Biomed. Opt. Princ. Imaging*, pp. 153–179, John Wiley & Sons, Inc. (2009).
[47] A. P. Gibson, J. C. Hebden, and S. R. Arridge, “Recent advances in diffuse optical imaging,” *Phys. Med. Biol.* **50**(4), R1 (2005) [doi:10.1088/0031-9155/50/4/R01].
[48] P. N. T. Wells, “Ultrasonic imaging of the human body,” *Rep. Prog. Phys.* **62**(5), 671 (1999) [doi:10.1088/0034-4885/62/5/201].
[49] L. V. Wang, “Multiscale photoacoustic microscopy and computed tomography,” *Nat. Photonics* **3**(9), 503–509 (2009) [doi:10.1038/nphoton.2009.157].
[50] X. Wang, G. Stoica, X. Xie, G. Ku, and L. V. Wang, “Noninvasive imaging of hemoglobin concentration and oxygenation in the rat brain using high-resolution photoacoustic tomography,” *J. Biomed. Opt.* **11**(2), 024015–024015–9 (2006) [doi:10.1117/1.2192804].
[51] L. Feeney, “Lipofuscin and melanin of human retinal pigment epithelium. Fluorescence, enzyme cytochemical, and ultrastructural studies.,” *Invest. Ophthalmol. Vis. Sci.* **17**(7), 583–600 (1978).
[52] M. Rajadhyaksha, M. Grossman, D. Esterowitz, R. H. Webb, and R. R. Anderson, “In vivo confocal scanning laser microscopy of human skin: melanin provides strong contrast,” *J. Invest. Dermatol.* **104**(6), 946–952 (1995).
[53] C. Tang, W. R. Bosenberg, T. Ukachi, R. J. Lane, and L. K. Cheng, “Optical parametric oscillators,” *Proc. IEEE* **80**(3), 365–374 (1992) [doi:10.1109/5.135353].
[54] A. E. Siegman, *Lasers*, University Science Books (1986).
[55] B. T. Cox, S. Kara, S. R. Arridge, and P. C. Beard, “k-space propagation models for acoustically heterogeneous media: application to biomedical photoacoustics,” *J. Acoust. Soc. Am.* **121**(6), 3453–3464 (2007) [doi:10.1121/1.2717409].
[56] P. Kuchment and L. Kunyansky, “Mathematics of thermoacoustic tomography,” *Eur. J. Appl. Math.* **19**(02), 191–224 (2008) [doi:10.1017/S0956792508007353].
[57] M. p. Birch, J. f. Messenger, and A. g. Messenger, “Hair density, hair diameter and the prevalence of female pattern hair loss,” *Br. J. Dermatol.* **144**(2), 297–304 (2001) [doi:10.1046/j.1365-2133.2001.04018.x].
[58] A. Ng and J. Swanevelder, “Resolution in ultrasound imaging,” *Contin. Educ. Anaesth. Crit. Care Pain*, mkr030 (2011) [doi:10.1093/bjaceaccp/mkr030].
[59] M. Xu and L. V. Wang, “Analytic explanation of spatial resolution related to bandwidth and detector aperture size in thermoacoustic or photoacoustic reconstruction,” *Phys. Rev. E* **67**(5), 056605 (2003) [doi:10.1103/PhysRevE.67.056605].
[60] A. Jemal, F. Bray, M. M. Center, J. Ferlay, E. Ward, and D. Forman, “Global cancer statistics,” *CA. Cancer J. Clin.* **61**(2), 69–90 (2011) [doi:10.3322/caac.20107].
[61] Canadian Cancer Society’s Advisory Committee on Cancer Statistics, “Canadian Cancer Statistics 2013,” Toronto, ON, Canadian Cancer Society (2013).
[62] S. R. Denmeade and J. T. Isaacs, “A history of prostate cancer treatment,” *Nat. Rev. Cancer* **2**(5), 389–396 (2002) [doi:10.1038/nrc801].
[63] M. R. Cooperberg, D. P. Lubeck, M. V. Meng, S. S. Mehta, and P. R. Carroll, “The Changing Face of Low-Risk Prostate Cancer: Trends in Clinical Presentation and Primary Management,” *J. Clin. Oncol.* **22**(11), 2141–2149 (2004) [doi:10.1200/JCO.2004.10.062].

[64] B. H. Han, K. Wallner, G. Merrick, W. Butler, S. Sutlief, and J. Sylvester, "Prostate brachytherapy seed identification on post-implant TRUS images," *Med. Phys.* **30**(5), 898–900 (2003) [doi:10.1118/1.1568976].
[65] S. A. McAleavey, S. White, and M. Menon, "2K-3 Magnetically Vibrated Brachytherapy Seeds: Ferromagnetic Core Models and Image Reconstruction Methods," in *IEEE Ultrason. Symp. 2006*, pp. 1103–1106 (2006) [doi:10.1109/ULTSYM.2006.283].
[66] D. R. Holmes III and R. A. Robb, "Improved automated brachytherapy seed localization in trans-urethral ultrasound data," 2004, 353–360 [doi:10.1117/12.535865].
[67] E. E. Connor, J. Mwamuka, A. Gole, C. J. Murphy, and M. D. Wyatt, "Gold Nanoparticles Are Taken Up by Human Cells but Do Not Cause Acute Cytotoxicity," *Small* **1**(3), 325–327 (2005) [doi:10.1002/smll.200400093].
[68] K. Homan, J. Shah, S. Gomez, H. Gensler, A. Karpiouk, L. Brannon-Peppas, and S. Emelianov, "Silver nanosystems for photoacoustic imaging and image-guided therapy," *J. Biomed. Opt.* **15**(2) (2010) [doi:10.1117/1.3365937].
[69] S. Mallidi, T. Larson, J. Tam, P. P. Joshi, A. Karpiouk, K. Sokolov, and S. Emelianov, "Multiwavelength Photoacoustic Imaging and Plasmon Resonance Coupling of Gold Nanoparticles for Selective Detection of Cancer," *Nano Lett.* **9**(8), 2825–2831 (2009) [doi:10.1021/nl802929u].
[70] S. A. Maier, *Plasmonics: Fundamentals and Applications: Fundamentals and Applications*, Springer (2007).
[71] S. Manohar, C. Ungureanu, and T. G. Van Leeuwen, "Gold nanorods as molecular contrast agents in photoacoustic imaging: the promises and the caveats," *Contrast Media Mol. Imaging* **6**(5), 389–400 (2011) [doi:10.1002/cmmi.454].
[72] L. V. Wang, *Photoacoustic Imaging and Spectroscopy*, CRC Press (2009).
[73] B. Wen, C. Liu, and Y. Liu, "Depositional Characteristics of Metal Coating on Single-Crystal TiO2 Nanowires," *J. Phys. Chem. B* **109**(25), 12372–12375 (2005) [doi:10.1021/jp050934f].
[74] L. M. Liz-Marz án and I. Lado-Touriño, "Reduction and Stabilization of Silver Nanoparticles in Ethanol by Nonionic Surfactants," *Langmuir* **12**(15), 3585–3589 (1996) [doi:10.1021/la951501e].
[75] CRC Press LLC, *CRC handbook of chemistry and physics*, CRC Press, Cleveland, Ohio (1977).
[76] M. Moradi, P. Mousavi, and P. Abolmaesumi, "Computer-Aided Diagnosis of Prostate Cancer with Emphasis on Ultrasound-Based Approaches: A Review," *Ultrasound Med. Biol.* **33**(7), 1010–1028 (2007) [doi:10.1016/j.ultrasmedbio.2007.01.008].
[77] M. Inahara, H. Suzuki, H. Nakamachi, N. Kamiya, M. Shimbo, A. Komiya, T. Ueda, T. Ichikawa, K. Akakura, et al., "Clinical evaluation of transrectal power Doppler imaging in the detection of prostate cancer," *Int. Urol. Nephrol.* **36**(2), 175–180 (2004) [doi:10.1023/B:UROL.0000034664.39784.33].
[78] F. L. Lizzi, E. J. Feleppa, S. Kaisar Alam, and C. X. Deng, "Ultrasonic spectrum analysis for tissue evaluation," *Pattern Recognit. Lett.* **24**(4–5), 637–658 (2003) [doi:10.1016/S0167-8655(02)00172-1].

[79] M. F. Insana, T. J. Hall, and L. T. Cook, “Backscatter coefficient estimation using array transducers,” *IEEE Trans. Ultrason. Ferroelectr. Freq. Control* **41**(5), 714–723 (1994) [doi:10.1109/58.308508].
[80] C.-L. Tsai, J.-C. Chen, and W.-J. Wang, “Absorption properties of soft tissue constitutents in the 900- to 1340-nm region,” in *SPIE* **3257**, pp. 118–125 (1998) [doi:10.1117/12.306077].